



**UNIVERSIDAD DE INVESTIGACIÓN DE
TECNOLOGÍA EXPERIMENTAL YACHAY**

Escuela de Ciencias de la Tierra, Energía Y Ambiente

**TÍTULO: CRUSTAL STRUCTURE OF EASTERN
BANGLADESH FROM AMBIENT NOISE
TOMOGRAPHY**

Trabajo de titulación presentado como requisito para la
obtención de título de Geología

Autor:

Harvey Andrés Reascos Recalde

Tutor:

Ph.D. Anna Foster

Cotutor:

Ph.D. Rafael Almeida

Urcuquí, Abril de 2021

SECRETARÍA GENERAL
(Vicerrectorado Académico/Cancillería)
ESCUELA DE CIENCIAS DE LA TIERRA, ENERGÍA Y AMBIENTE
CARRERA DE GEOLOGÍA
ACTA DE DEFENSA No. UITEY-GEO-2021-00005-AD

En la ciudad de San Miguel de Urququí, Provincia de Imbabura, a los 25 días del mes de junio de 2021, a las 10:30 horas, en el Aula CHA-01 de la Universidad de Investigación de Tecnología Experimental Yachay y ante el Tribunal Calificador, integrado por los docentes:

| | |
|---------------------------------------|-------------------------------------|
| Presidente Tribunal de Defensa | Dr. MARTIN MERINO, GERMAN , Ph.D. |
| Miembro No Tutor | Dra. PIISPA , ELISA JOHANNA , Ph.D. |
| Tutor | Dra. FOSTER ANNA ELIZABETH , Ph.D. |

Se presenta el(la) señor(ita) estudiante **REASCOS RECALDE, HARVEY ANDRES**, con cédula de identidad No. **1003460605**, de la **ESCUELA DE CIENCIAS DE LA TIERRA, ENERGÍA Y AMBIENTE**, de la Carrera de **GEOLOGÍA**, aprobada por el Consejo de Educación Superior (CES), mediante Resolución **RPC-SE-10-No.031-2016**, con el objeto de rendir la sustentación de su trabajo de titulación denominado: **Crustal structure of eastern Bangladesh from ambient noise tomography.** , previa a la obtención del título de **GEÓLOGO/A**.

El citado trabajo de titulación, fue debidamente aprobado por el(los) docente(s):

| | |
|--------------|------------------------------------|
| Tutor | Dra. FOSTER ANNA ELIZABETH , Ph.D. |
|--------------|------------------------------------|

Y recibió las observaciones de los otros miembros del Tribunal Calificador, las mismas que han sido incorporadas por el(la) estudiante.

Previamente cumplidos los requisitos legales y reglamentarios, el trabajo de titulación fue sustentado por el(la) estudiante y examinado por los miembros del Tribunal Calificador. Escuchada la sustentación del trabajo de titulación, que integró la exposición de el(la) estudiante sobre el contenido de la misma y las preguntas formuladas por los miembros del Tribunal, se califica la sustentación del trabajo de titulación con las siguientes calificaciones:

| Tipo | Docente | Calificación |
|--------------------------------|-------------------------------------|--------------|
| Presidente Tribunal De Defensa | Dr. MARTIN MERINO, GERMAN , Ph.D. | 9,7 |
| Miembro Tribunal De Defensa | Dra. PIISPA , ELISA JOHANNA , Ph.D. | 9,6 |
| Tutor | Dra. FOSTER ANNA ELIZABETH , Ph.D. | 9,4 |

Lo que da un promedio de: **9.6 (Nueve punto Seis)**, sobre 10 (diez), equivalente a: **APROBADO**

Para constancia de lo actuado, firman los miembros del Tribunal Calificador, el/la estudiante y el/la secretario ad-hoc.

REASCOS RECALDE, HARVEY ANDRES
Estudiante

HARVEY
 ANDRES
 REASCOS
 RECALDE

Firmado digitalmente por HARVEY ANDRES REASCOS RECALDE
 Fecha: 2021.07.14 12:45:44 -05'00'

Dr. MARTIN MERINO, GERMAN , Ph.D.
Presidente Tribunal de Defensa

GERMAN
 MARTIN
 MERINO

Firmado digitalmente por GERMAN MARTIN MERINO
 Nombre de reconocimiento (DN): c=EC, o=BANCO CENTRAL DEL ECUADOR, ou=ENTIDAD DE CERTIFICACION DE INFORMACION ECRICE, l=QUITO, serialNumber=000236837, cn=GERMAN MARTIN MERINO
 Fecha: 2021.07.13 10:32:34 -05'00'

Dra. FOSTER ANNA ELIZABETH , Ph.D.
Tutor

ANNA
 ELIZABETH
 FOSTER

Digitally signed by ANNA ELIZABETH FOSTER
 Date: 2021.07.13 12:29:47 -05'00'

Dra. PIISPA , ELISA JOHANNA , Ph.D.
Miembro No Tutor

Digitally signed by
ELISA JOHANNA PIISPA

TERÁN ROSALES, ANDREA YOLANDA
Secretario Ad-hoc

ANDREA
YOLANDA
TERAN ROSALES

Firmado digitalmente
por ANDREA YOLANDA
TERAN ROSALES
Fecha: 2021.06.25
21:04:48 -05'00'

AUTORÍA

Yo, **Harvey Andrés Reascos Recalde**, con cédula de identidad 1003460605, declaro que las ideas, juicios, valoraciones, interpretaciones, consultas bibliográficas, definiciones y conceptualizaciones expuestas en el presente trabajo; así cómo, los procedimientos y herramientas utilizadas en la investigación, son de absoluta responsabilidad de el/la autor (a) del trabajo de integración curricular. Así mismo, me acojo a los reglamentos internos de la Universidad de Investigación de Tecnología Experimental Yachay.

Urcuquí, junio del 2021.

Harvey Andrés Reascos Recalde

CI: 1003460605

AUTORIZACIÓN DE PUBLICACIÓN

Yo, **Harvey Andrés Reascos Recalde**, con cédula de identidad 1003460605, cedo a la Universidad de Investigación de Tecnología Experimental Yachay, los derechos de publicación de la presente obra, sin que deba haber un reconocimiento económico por este concepto. Declaro además que el texto del presente trabajo de titulación no podrá ser cedido a ninguna empresa editorial para su publicación u otros fines, sin contar previamente con la autorización escrita de la Universidad.

Asimismo, autorizo a la Universidad que realice la digitalización y publicación de este trabajo de integración curricular en el repositorio virtual, de conformidad a lo dispuesto en el Art. 144 de la Ley Orgánica de Educación Superior

Urcuquí, junio del 2021.

Harvey Andrés Reascos Recalde

CI: 1003460605

DEDICATION

I want to dedicate it to my parents, Consuelo Recalde and Harvey Reascos, who always support me and help me with the resources to keep studying during all career. They always inspired and believe in me. I also dedicate it to my sister, Pamela Reascos, and my brother, Bryan Reascos, who also believe in me and inspired me to try and get new things.

Best,

HARR

ACKNOWLEDGMENTS

I want to give my sincere gratitude to my advisor Anna Foster, Ph.D., for her patience, help, and guidance during my thesis work. She shared a lot of new knowledge about seismic topics with me, so as a consequence, I started to love more this science branch. Without her support and inspiration to me, it would be tough for me. Also, I want to thank my co-advisor, Rafael Almeida, Ph.D., who taught me many things about Bangladesh's structural geology and guidance me with my thesis work. In a general way, I want to thank all my professors during my career who taught me a lot about geology in the world, especially from Ecuador. Furthermore, they made me grow as a person because I acquired many experiences during field works throughout the career. Then, I want to express my gratitude to all my "geo-mates" because they were like a second family who supports me all time and shared many great moments.

Finally, I want to give all my gratitude to my mother, Consuelo Recalde, and my father, Harvey Reascos, who support me during my whole stay at the university. They motivated me to continue studying despite adversity. I am proud of them because they are fighters!

HARR

ABSTRACT

Imaging the crustal structure from the cross-correlation of ambient seismic noise is a useful seismic method. Here we show a considerable study of Eastern Bangladesh using the seismic network "Temporary Receivers for Monitoring Bangladesh Earthquakes," a total of 22 short-period seismometers and six broadband seismometers deployed by the Earth Observatory of Singapore and Dhaka University from 2016 to the present. We also test broadband data from other networks located in Myanmar and India. Applying some methods to the different wave components, we find that from the vertical component, we can retrieve the Green's functions by cross-correlations corresponding to Rayleigh waves, and generate phase velocity images. Rayleigh wave phase velocities are extracted between 2 – 10 s period. These measurements are inverted to produce phase velocity maps on a $0.25^\circ \times 0.25^\circ$ grid using a 2-D tomographic scheme. Because Bangladesh is affected by the interactions of three tectonic plates: Indian, Eurasian, and Burma, it results in complex fault systems. Along our zone of study, we can differentiate some geological features like faults and sedimentary basins. At the shortest periods in the north group stations, the phase velocity could be associated with the Sylhet Basin, and the change in wavespeed from west to east maybe match the Sylhet Fault. Also, for the shortest periods in the south group station the wavespeeds could be related with the Chin Hills and the Kaladan Fault. At the largest periods in the north group stations, the wavespeeds are similar to the shortest periods, so they could also match the Sylhet Basin. In the south group stations, the wavespeeds could be associated with the Tripura Fold Belt. The sensitivity of these waves reaches a depth of ~20 km, so the wavespeeds might be related to the thick sedimentary layer, and also, the changes in phase velocity from west to east might represent the Indo-Burma subduction zone.

Key words: *Tomography, Green's Function, Spectral Density, Coherency, Phase Velocity, Bessel Function.*

RESUMEN

Obtener imágenes de la estructura de la corteza terrestre a partir de la correlación cruzada del ruido sísmico ambiental es un método sísmico útil. Aquí mostramos un estudio considerable del este de Bangladesh utilizando de la red sísmica "Receptores Temporales Para Monitorear Terremotos de Bangladesh" TREMBLE por sus siglas en inglés, un total de 22 sismómetros de período corto y seis sismómetros de banda ancha desplegados por el Observatorio de la Tierra de Singapur (Earth Observatory of Singapore en inglés) y la Universidad de Dhaka desde 2016 hasta el presente. También probamos datos de banda ancha de otras redes ubicadas en Myanmar e India. Aplicando varios métodos a los distintos componentes de onda, encontramos que a partir del componente vertical, podemos recuperar las funciones de Green mediante correlaciones cruzadas que corresponden a las ondas de Rayleigh, y después, generar imágenes de velocidad de fase. Las velocidades de fase de la onda de Rayleigh se extraen entre un período de 2 a 10 s. Estas medidas se invierten para producir mapas de velocidad de fase en una cuadrícula de $0,25^\circ \times 0,25^\circ$ utilizando un esquema tomográfico 2-D. Debido a que Bangladesh se ve afectado por las interacciones de tres placas tectónicas: India, Eurasia y Burma, esto resulta en complejos sistemas de fallas. A lo largo de nuestra zona de estudio, podemos diferenciar algunas características geológicas como fallas y cuencas sedimentarias. En los períodos más cortos en las estaciones del grupo norte, la velocidad de fase podría estar asociada con la cuenca de Sylhet, y el cambio en la velocidad de onda de oeste a este puede coincidir con la falla de Sylhet. Además, durante los períodos más cortos en las estaciones del grupo sur, las velocidades de las ondas podrían estar relacionadas con las colinas de Chin y la falla de Kaladan. En los períodos más grandes en las estaciones del grupo norte, las velocidades de las ondas son similares a los períodos más cortos, por lo que también podrían coincidir con la Cuenca Sylhet. En las estaciones del grupo sur, las velocidades de onda podrían estar asociadas con el Cinturón Plegable de Tripura. La sensibilidad de estas ondas alcanza una profundidad de ~ 20 km, por lo que las velocidades de las ondas pueden estar relacionadas con una capa sedimentaria gruesa y, los cambios en la velocidad de fase de oeste a este podrían representar la zona de subducción de Indo-Burma.

Palabras clave: tomografía, función de Green, densidad espectral, coherencia, velocidad de fase, función de Bessel.

TABLE OF CONTENTS

| | |
|---|------|
| DEDICATION | V |
| ACKNOWLEDGMENTS | VI |
| ABSTRACT | VII |
| RESUMEN | VIII |
| CHAPTER 1. INTRODUCTION..... | 1 |
| 1.1 Bangladesh..... | 1 |
| 1.2 Seismic methods..... | 2 |
| 1.3 Ambient seismic noise..... | 4 |
| 1.4 Ambient noise tomography | 5 |
| 1.5 Objectives | 6 |
| CHAPTER 2. TECTONIC AND GEOLOGICAL SETTING | 7 |
| 2.1 Large scale tectonics..... | 7 |
| 2.2 Indo-Burma Range | 8 |
| 2.3 Stratigraphy | 10 |
| 2.4 Previous geophysical studies | 12 |
| CHAPTER 3. DATA..... | 13 |
| CHAPTER 4. METHODS..... | 16 |
| 4.1 Preprocessing methods | 17 |
| 4.2 Phase velocity measurements | 18 |
| 4.3 Tomography | 20 |
| CHAPTER 5. RESULTS..... | 21 |
| 5.1 Preparing data..... | 21 |
| 5.2 Comparison of preprocessing methods..... | 22 |
| 5.3 Phase velocity measurements and Bessel function | 27 |
| 5.4 Rayleigh wave phase velocity maps..... | 30 |
| CHAPTER 6. DISCUSSION | 34 |

| | |
|--|----|
| 6.1 Quality of data | 34 |
| 6.2 Interpretation of phase velocity maps..... | 35 |
| CHAPTER 7. CONCLUSIONS | 38 |
| 7.1 Future work | 39 |
| REFERENCES | 40 |
| ANNEX | 45 |
| Annex 1. Data preparation code | 45 |

TABLE OF FIGURES

| | |
|---|----|
| Figure 1 Major geological features and seismic station locations..... | 1 |
| Figure 2 Regional tectonic setting of Bangladesh | 9 |
| Figure 3 Delta representation of Ganges-Brahmaputra Delta and cross-section with major geological features..... | 11 |
| Figure 4 Seismic station locations from both broadband and short-period stations..... | 13 |
| Figure 5 Continuous data for short period stations | 21 |
| Figure 6 Continuous data for broadband stations..... | 22 |
| Figure 7 Coherency plots for short-period stations | 23 |
| Figure 8 Coherency plots for broadband stations..... | 24 |
| Figure 9 Cross-spectra and signal to noise ratio for short-period stations. | 25 |
| Figure 10 Cross-spectra and signal to noise ratio for broadband stations..... | 26 |
| Figure 11 Power spectral density for all short period stations. | 27 |
| Figure 12 Group velocity window for short-period stations | 28 |
| Figure 13 Real (top) and imaginary (middle) cross spectra in the vertical component.. | 29 |
| Figure 14 Cross-correlation function and corresponding SNR (top), fit of the J_0 Bessel function (red line) with the cross-spectrum (black line)..... | 30 |
| Figure 15 Ray density at different periods (approximately 2, 4, 6, and 10 s)..... | 31 |
| Figure 16 Phase velocity maps at different periods (approximately 2, 4, 6, and 10 s)... | 32 |
| Figure 17 Average Isotropic Phase Velocity dispersion curve for all periods in a range from 2-10s | 33 |
| Figure 18 Sensitivity Kernel for Rayleigh waves..... | 37 |

TABLE OF TABLES

| | |
|---|----|
| Table 1. Data for all seismic stations..... | 14 |
|---|----|

CHAPTER 1. INTRODUCTION

The United Nations' Asia Pacific Disaster Report of 2015 puts Bangladesh in the 10th place in the world where natural disasters occur and 5th place in the world for risk (UNESCAP, 2015). The country is situated where three tectonic plates meet, Indian, Eurasia, and Burma, making it a tectonically active region with many faults (Figure 1 and Figure 2). Because of this, Bangladesh is in a zone with a high potential for seismic hazards, threatening a high-density and low-income population. Furthermore, the country is affected by other natural disasters like floods, riverbank erosion, and droughts. Also, at the west part of the IBR, from 17°N - 25°N occur many landslides. These features make Bangladesh a critical location for a good analysis of the crustal structure to better characterize the sediment layers, depth to basement rocks, and recognize faults (Zaman et al., 2018).

1.1 Bangladesh

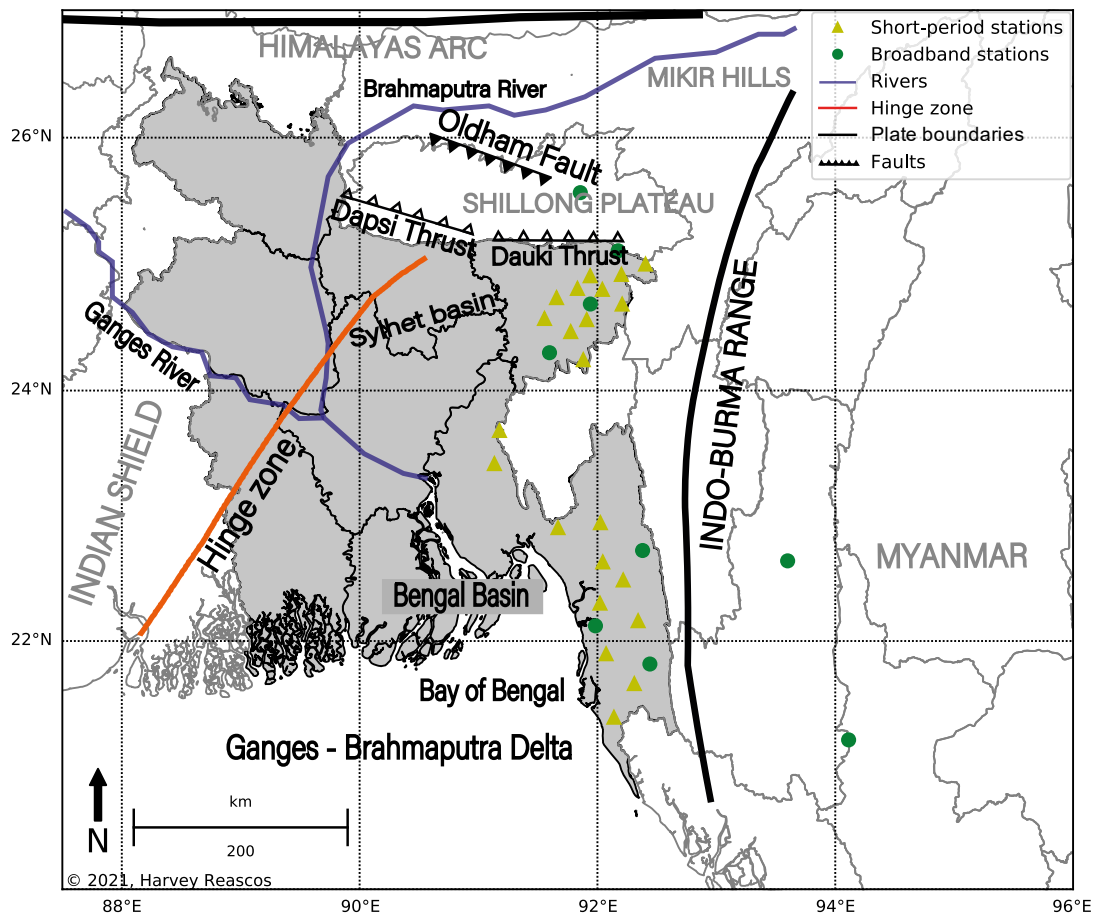


Figure 1 Major geological features and seismic station locations. Bangladesh (gray) is bordered by the Indian Shield to the west, the Shillong Plateau and Mikir Hills to the northeast, and the Indo-Burma range to the east. Known faults in the northeast (Oldham, Dapsi, and Dauki) are

displayed. Two main rivers carry sediments to the Ganges-Brahmaputra Delta from the Himalayan Arc (at the north). The hinge zone separates the thick continental crust from the thinned continental margin crust. Seismic stations for our study are located in the eastern part. Geological features extracted from Singh et al. (2016b).

Bangladesh is bordered mainly by India and in a few parts by Myanmar (Zaman et al., 2018). Its location is between the Indian shield in the west, the Mikir Hills and Shillong plateau to the northeast, and the Indo-Burmese subduction zone to the east (Figure 1). Moreover, the transition zone from thick continental crust to thinned is known as the Hinge zone, with an orientation of NNE-SSW, representing the trace of the Eocene continental shelf edge and dividing the country into two tectonic units, the geosynclinal basin to the southeast and the Pre-Cambrian platform to the northwest (Rashid, 2014). Since the Eocene, the Geosynclinal Basin (GB) has filled an area of 300-400 km length from the Hinge zone to its present extent by sediments from the Himalaya, carried mainly by Brahmaputra and Ganges rivers (Rashid, 2014).

This GB is one of the largest geosynclinal basins globally, and it includes both the Bengal Basin and the Bay of Bengal (Rashid, 2014). The Bengal Basin is a region conformed mainly by sediments with a thickness of approximately 12 - 20 km. This zone is affected at the northern part by the Shillong Plateau, which overthrusts it, causing a depression of the Sylhet Basin and increasing its thickness by ~12 - 16 km (Singh et al., 2016; Johnson & Nur Alam, 1991). At the south, there is the Ganges-Brahmaputra Delta (GBD) traversed by an active plate boundary where both earthquakes and aseismic activity occur. The Sumatra-Andaman earthquake in 2004 shook the GBD and put Bangladesh at a higher risk for earthquakes (Steckler et al., 2008). These geological features and seismic activity demonstrate the necessity of applying seismic methods and studying seismic waves to create maps that help us understand the continental structure and layer depths.

1.2 Seismic methods

As we mentioned before, sediments that filled Bangladesh come from the Himalayas; the Himalayas' topography also results in high precipitation, surface run-off, and flooding in the lower reaches. This makes it challenging to study the features mentioned above at the surface. An alternative is to apply different seismic methods to obtain good surface and crustal structure models (e.g., MoDMER, 2015; Rabbel, 2006;

Stoker et al., 1997).

The majority of seismic methods use signals generated by earthquakes and human-made sources. The signals produce different types of waves: body waves, which go through the Earth's body, and surface waves, which travel along the Earth's surface. Body waves can be divided into P-waves (pressure waves), known as primary because they are the fastest, and S-waves (shear waves), known as secondary because they are slowest. Surface waves consist of Love waves and Rayleigh waves (Rabbel, 2006). The seismic wave velocities are related to the rock directly by the density and elasticity of the medium and indirectly to composition and temperature. Also, the density and the elastic properties depend on the temperature and composition of the rock, which varies at depth. As well, the wave velocity measurements provide essential information on the design of both continental and oceanic crust (Condie, 2016). For this reason, the study of seismic wave velocities is a practical approach to high-quality imagery of the crustal structure of Bangladesh.

In Ammon (2019), P-waves or compressional waves travel at a speed between 1 and 14 km/s in the same direction of the wave propagation. The slower velocity is when traveling on water and the higher is when traveling into the Earth's mantle. S-waves or shear waves have a speed of 1 to 8 km/s and travel perpendicular to the direction of propagation. The slower velocity corresponds to waves on unconsolidated sediments and the higher rate near the Earth's mantle, and it doesn't propagate through gas or fluids. Love waves are transverse waves resulting from S-waves' interaction with the Earth's surface, and they travel horizontally perpendicular to the wave propagation. They travel between 2 to 6 km/s, and their velocity decrease with depth. Rayleigh waves are the slowest waves with speed from 1 to 5 km/s, and they decrease their amplitude with depth. The fact that waves travel at different velocities depending on the material properties allows us to use seismic methods to investigate Earth's structure (Ammon, 2019). Then, the dispersion of surface waves gives information of the shear-wave velocity in the uppermost mantle (Rivet et al., 2015).

Many seismic methods are helpful to study the structure of the crust. These techniques use active and passive sources of energy. The active source methods require human activity, such as air guns, seismic vibrators, borehole explosions, etc. Passive sources are those that occur by natural seismicity. Two essential categories utilize human-made sources; seismic refraction/wide-angle reflection profiles bring decent information

about the crust's seismic velocities distribution. They are handy to map the crust's thickness, and near-vertical incidence seismic reflection profiles grant detailed crustal imagery at a finer scale (e.g., Artemieva & Meissner, 2012; Rabbel, 2006; Stoker et al., 1997).

On the other hand, passive techniques include seismic tomography, seismic receiver functions, and seismic ambient noise inversion. Seismic tomography uses arrival times of crossed paths between the seismometers and the earthquakes to obtain a 3-D image of the Earth's crustal. Seismic receiver functions use broadband stations, and the processing of three components determines the crust's layer boundaries by using teleseismic P-wave conversion arrivals. Ambient noise analysis, which has no earthquake dependence, focuses on the cross-correlation of station pairs to retrieve the waves' velocity. Then, an inversion method helps us to obtain crustal structure images (Mooney, 2015). We will describe ambient seismic noise in more detail in the following sections.

1.3 Ambient seismic noise

Ambient seismic noise comprises various signals covering a range of frequencies, including ocean waves, glaciers, climate, ship wakes, solar forcing, and wind waves (Yang & Ritzwoller, 2008). Broadband seismometers can record seismic noise at frequencies ranging from a few milli Hz to tens of Hz. The ambient noise recorded at short periods, mainly between 0.1 - 1 s, is generated from human activity from the electrical grid, trains, cars, and machinery near the seismic stations. At intermediate periods, between 1 - 30 s, the microseism generates a higher amplitude of noise than in other parts of the seismic spectrum. The microseism band can be broken down into primary and secondary microseisms. The primary microseism is strongest on frequencies between 0.05 Hz and 0.08 Hz, and it is related to ocean gravity waves when they arrive and break on the seafloor's offshore or slope. The secondary microseism, which is prevalent at frequencies from 0.1 Hz to 0.16 Hz, is generated mainly by the shock of two ocean waves traveling in different directions and similar frequencies (Schimmel et al., 2011). Noise at long periods, 30 - 500 s, are signals produced by infragravity of the oceans caused by storms or winds (Physics, 2019). The weakest signal is the "hum," which consists mainly of free oscillations of the Earth from 5 - 20 mHz, and the strongest signal is the microseism, which is predominantly Rayleigh waves measured from 0.04 - 1 Hz (Schimmel et al., 2011).

The advantage of using ambient seismic noise as an energy source is that studies are no longer limited to high seismicity regions. Furthermore, it helps make measurements at short periods, which are not possible using teleseismic observations. For that, it is efficient to generate high-resolution seismic continental structure maps in any region (Sadeghisorkhani, 2017). Ambient seismic noise does not depend on the Earth's landscape. We will explain it in more detail in the following sections.

1.4 Ambient noise tomography

Ambient noise contains information about the Earth's structure, and according to Saygin & Kennett (2010), we can access that information using data derived from the cross-correlation of ambient noise between different station pairs. The raw data consists of continuous recordings of the noise field between two stations, separated by some distance. This noise field's cross-correlation allows us to find the elastic impulse response (Green's Function) (Saygin & Kennett, 2010).

Greens' Function (GF) represents the Earth's response to an impulse of energy, and from this, we can estimate the Rayleigh wave phase velocity and generate high-resolution phase velocity maps (Yang & Ritzwoller, 2008). These 2-D images represent the phase velocity at different frequencies, which corresponds to different crustal depths (Saygin & Kennett, 2010). The spatial length of ambient noise tomography typically is local or regional, depending on the period (Ritzwoller et al., 2011).

Surface waves provide information about the shear wave velocities in the uppermost Earth's layers, and they are easily retrieved from ambient noise cross-correlation. Surface waves are beneficial for ambient noise cross-correlation because ambient noise sources are generated principally by atmospheric and oceanic interactions with the Earth's surface. The surface waves dominate the Green's Function for station pairs at Earth's surface (Rivet et al., 2015). These results allow us to generate different phase velocity maps at different periods to analyze the crustal structure and differentiate sedimentary layers or geological features.

In addition to surface wave velocities, body wave velocities can also be measured using cross-correlation of noise. However, body waves in ambient noise are limited in some frequency ranges, azimuthally heterogeneous, and weaker. For that, it is necessary to apply a spatial coherency of body waves between the receivers. This is because the body wave signals are weak in each correlation function, and the averaging of long

periods can cause the body wave extraction to be laborious (Nakata et al., 2019).

1.5 Objectives

We want to generate high-quality phase velocity maps at different periods in Eastern Bangladesh, where there are thick layers of sediments. Because of the seismic events that occur by the convergence zone in the Indo-Burma range and the present offshore to the southeast, much seismic noise is generated in this area (Rivet et al., 2015), which are seismic signals we will use to do our study. For that, this study aims to analyze six months of seismic noise data by making cross-correlations of all possible station pairs to get the Green's Function. We will make measurements of the phase velocity from the Green's Function and then invert the measurements to get phase-velocity maps. This method will serve as a critical test case for the technique of ambient noise tomography in Bangladesh, which has not been previously applied. We will interpret the phase velocity maps in terms of crustal structure, focusing mainly on sediment layers, depth of the basement rocks, and recognizing faults in the area. Furthermore, with this study, we want to make people aware of the risks and hazards of earthquakes after knowing where the seismic waves travel faster.

CHAPTER 2. TECTONIC AND GEOLOGICAL SETTING

2.1 Large scale tectonics

Bangladesh lies near the junction of three tectonic plates, the Indian, Eurasian, and Burmese plates. These result in two convergent boundaries, the India-Eurasia to the north, forming the Himalaya arc, and the India-Burmese to the east, including the Burma arc or Indo-Burma range (Figure 1). The Indian Plate moves northward at a rate of approx. 60 mm/yr. This event results in convergence at a rate of 45 mm/yr to the north with the Eurasian Plate and 35 mm/yr with the Burmese Plate to the east. The convergence of the Indian Plate at the Indo-Burma Range (IBR) is highly oblique. This margin can result in a partitioning into two plate motion components, one parallel and one normal to the boundary (Sarraz, 2015). Additionally, we can infer that convergence occurs by slip partitioning in this active plate after analyzing the faults that define an oblique motion between two plates that move in different directions (Toda et al., 2016).

Furthermore, structural analysis shows strike-slip movement within the inner belt of the IBR. Because of the presence of active deformation between eastern Bangladesh and the Shan Plateau in western Myanmar (Figure 2), many dextral shear events result in north-striking right-lateral faults in the inner belt, including the Churachandpur-Mao Fault (CMF) with an extension ~800 km from southeast-northeast of Bangladesh, and Sagaing fault (Figure 2). The study made by Betka et al. (2018) shows that the eastward section of the oblique plate convergence is partitioned to the up-dip part of the IBR (Naga Hills in Figure 2) and includes the blind and outer belts (Figure 2), resulting in the formation of antiforms. The blind belt is the area where we cannot distinguish antiforms at the surface, and the outer belt is the zone where we can differentiate the antiforms above the surface (Betka et al., 2018).

Active faults resulting from this continuous oblique convergence can host mild to great earthquakes (Sarraz, 2015). Bangladesh is bounded to the north by the Naga and Dauki Fault Thrust (DFT); the latter has an extension of 300 km east-west. In Sarraz (2015), the DFT is along the Shillong Plateau's southern edge. The Shillong Plateau uplifted during the Pliocene-Pleistocene, which in Ismal & Alam (2009) suggest that it results from the bound of two reverse faults; at the north, the Oldham fault, and at the south the Dauki Fault. The Gumti Fault is reported to extend from the southwest to the northeast (Rakshit et al., 2018). The Sylhet Fault (SF) has a parallel trend to this within the country with an extension of 150 km (Alam & Dominey-Howes, 2014). To the east,

within the fold and thrust belt, there are several thrust and strike-slip faults that build up the IBR. These will be described in the following section. Finally, the subduction zone influences Bangladesh at its southern edge. There is the Arakan subduction zone at the south of Bangladesh, and at the northeast of the Naga-Haflong-Disang thrust zone (Figure 2) is the Assam basin. (Sarraz, 2015; Islam & Alam, 2009)

Within Bangladesh, the lithosphere is divided into two tectonic units, the Stable Precambrian Platform to the northwest and the GB to the southeast. These are separated by the hinge zone, which runs from the Northeast to Southwest with a width of 25 km. Sedimentary rocks of variable thickness characterize the Stable Precambrian Platform above a Precambrian igneous and metamorphic basement, and it is not affected by folding related to plate convergence. Nearly 20 km of sedimentary clastic rocks characterize the GB, mainly composed of shale and sandstone of Tertiary age. Two divisions represent the GB; (1) to the west, the foredeep has no appreciable folding features (for Betka et al. 2018, this is the blind belt). (2) To the east, the folding of sedimentary layers that form anticlines (upward folds) and synclines (downward folds) characterize the fold belt (for Betka et al., (2018), this is equivalent to the outer and the inner belts) (Islam & Alam, 2009). The folding of sedimentary layers results in the formation of the IBR.

2.2 Indo-Burma Range

The IBR is a fold-thrust belt with an N-S trend located between the Kabaw Fault and the outer belt. From north to south, the IBR subdivisions are Naga Hills, Manipur Hills, Chin Hills, and Arakan Hills (Acharyya, 2010). As previously mentioned, the IBR is a zone of strain partitioning: E-W shortening in the outermost (western) part and right-lateral shearing in the innermost (eastern) part. Dextral strike-slip faults characterize the thick-skinned deformation, e.g., the Chittagong Fault and the Kaladan Fault. These tectonic deformation changes are related to the indentation of Eurasia caused by the Indian Plate and its clockwise rotation (Maurin & Rangin, 2009). The IBR's width is approximately 150 km, and its average elevation is 1000 m (Region, 1984).

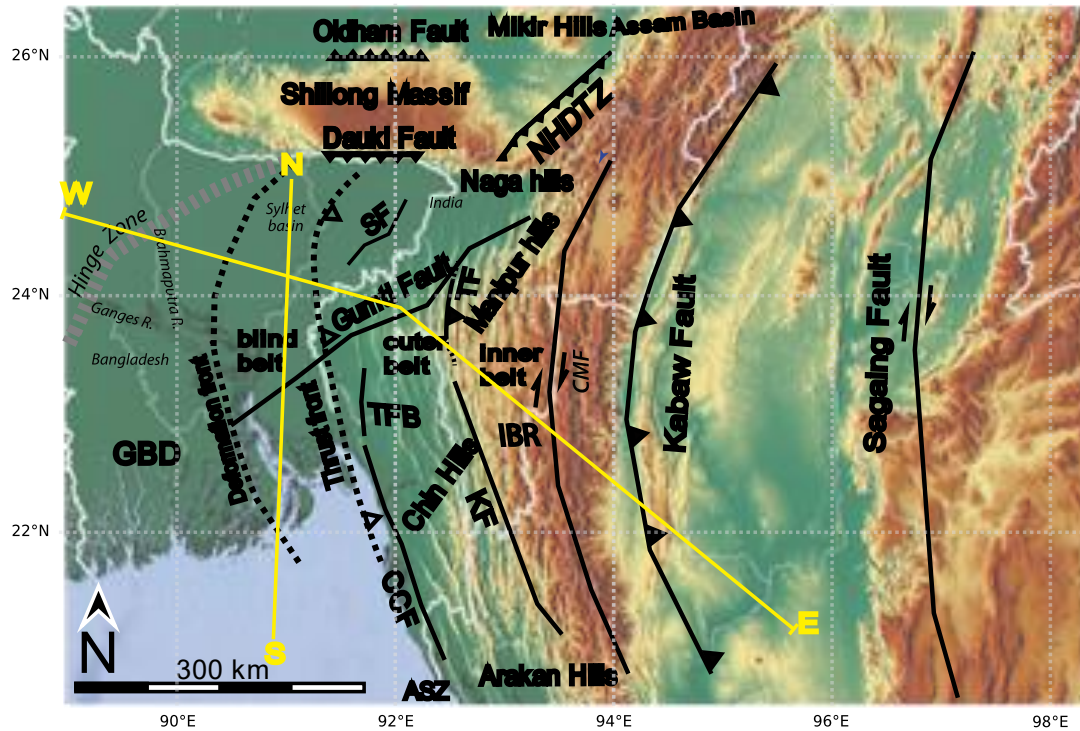


Figure 2 Regional tectonic setting of Bangladesh. Dashed lines represent the deformation front and the thrust front on both sides of the blind belt. The outer belt is separated from the inner belt by the Tut Fault (TF) and Kaladan Fault (KF) (Betka et al., 2018). Strike-slip (Churachandpur-Mao Fault, CMF; Sagaing Fault; Kaladan Fault) and thrust faults (Sylhet Fault, SF; Kabaw Fault, KF; Chittagong Coastal Fault, CCF; Naga-Haflong-Disang Thrust Zone, NHDTZ; Dauki Fault, DF) characterize the IBR. Tripura Fold Belt, TFB, in the outer belt. The Arakan Subduction Zone (ASZ) is located in southeast Bangladesh (Rakshit et al., 2018). The West-East and North-South section across the Bengal Basin showed in Figure 3 (Bandyopadhyay, 2019).

The direction of convergence between India and southeast Asia at the IBR is highly oblique, approx. 70° . According to Betka et al. (2018), where the subduction zone encounters the 12 - 20 km thick GBD, the IBR widens to $>300\text{km}$ to accommodate the massive sedimented margin. We can divide the IBR into the blind belt, the outer belt, and the inner belt, following Betka et al. (2018). In the blind belt is the Chittagong Coastal Fault which has a dextral transpressional deformation. The outer belt is affected mainly by a dextral transpressional deformation that is associated with the Chittagong-Myanmar fault. Here, the Kaladan Fault and the Churachandpur-Mao Fault (CMF) have a strike-slip motion. The inner belt is affected by right-lateral shear zones based on strike-slip centroid moments produced by intermediate earthquakes in the lower plate, such as the strike-slip Sagaing Fault. Additionally, in the inner belt, the Kabaw Fault is an east-

dipping oblique thrust fault (Rangin et al., 2013). These events are driven by gravity collapse, which results in the shortening of GBD over the blind and outer belts (Betka et al., 2018).

The IBR convergence rate is about 13 - 17 mm/y, but within the outer belt, the rate is >4.8 mm/y. It results in an estimated shortening of 38.4 km, also, a total underthrusting rate of ~19.8 mm/y for the sediments below the lower plate below the décollement. A décollement is a fault surface parallel to the bedding that detaches or separates deformed rocks above from undeformed rocks below. According to Steckler et al. (2016), in the IBR, only thick sediments and thin-crust enters the subduction zone, and the most unusual aspect of this subduction boundary is the thick sediments accreted. From Rangin et al. (2016), west of the CMF, there is a ~250 km wide Neogene accretionary prism built by thick sediments from the Bengal Basin and the GBD. An analysis by Betka et al. in 2018 used kinematic models to predict a décollement depth between 3.1 to 3.4 km below sea level. Also, the Accretionary Prism gradient varies from 0.1° in the forearc to 0.5° to the east, and the relationship between the low slope and the overpressured sediments results in a weak detachment (Steckler et al., 2008). This kinematic analysis also proves that the outer belt exhibits east-trending shortening in the fault-cored folds' axial trace. A study by Rangin et al. in 2013 of intermediate seismicity (30 – 100 km) illustrates that the strike-slip and normal faulting inside the deeper subducted crust is decoupled from the east-trending shortening of the upper Plate.

2.3 Stratigraphy

The GBD controls the stratigraphy of the region. When rivers empty their sediments and water into another water body, such as lakes, oceans, or other rivers, they form deltas. Two divisions characterize deltas; the subaqueous and the subaerial. The subaqueous division is underwater and the steepest part of the delta, which contains the finest silt (Figure 3, Figure 4). The furthest part of the river's mouth or the newest part of the subaqueous is the pro-delta. The subaerial division is above water, and the part most influenced by tides and waves is the lower delta. The region affected by the river's flow is the upper delta (Society, 2020). In this case, the GBD was formed by the country's two main rivers, as the GBD name indicated, the Ganges and Brahmaputra rivers. The first input of sediments was by the Brahmaputra during the Early Miocene before the uplift of the Shillong Plateau. During the Neogene, the colliding plates uplifted the Shillong Plateau, which changed the Brahmaputra's course to the west (Betka et al., 2018). The

Ganges and Brahmaputra rivers discharge farther east into a recess in the coastline between the subduction zone and the delta (Figure 1). With time, this embayment will close because of the subduction of the delta with the Burma Arc.

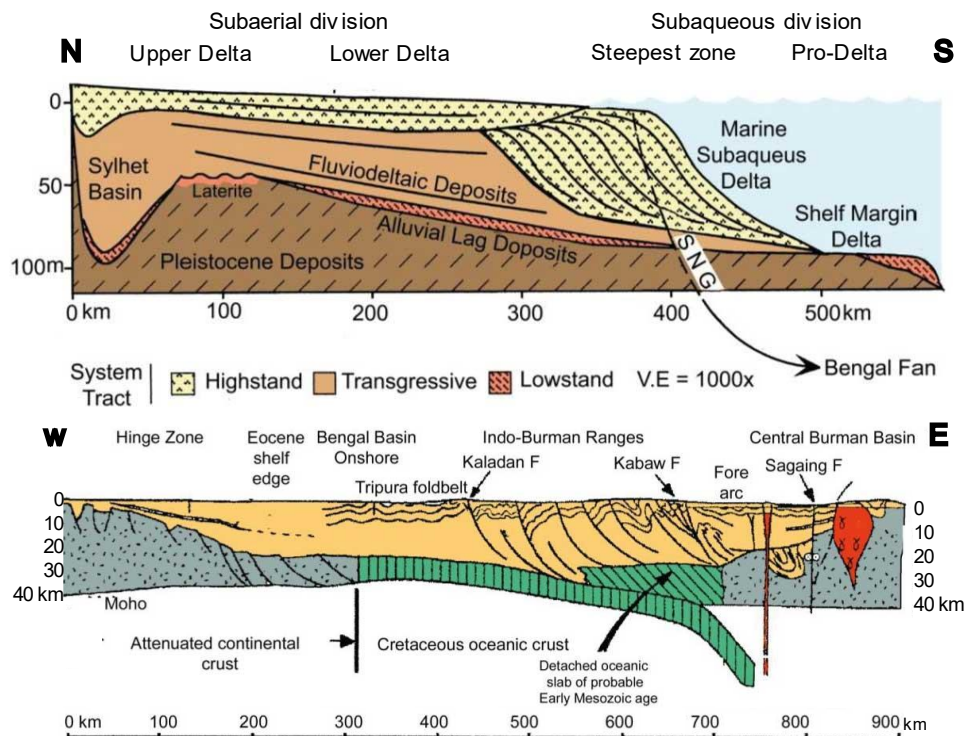


Figure 3 Delta representation of Ganges-Brahmaputra Delta and cross-section with major geological features. Top: representation of the structure of a delta, which corresponds qualitatively to the stratigraphic sequences found from the Sylhet Basin to the GBD; from north to south, we can distinguish the Delta Plain, Marine Subaqueous Delta, and the Shelf Margin Delta. Bottom: crustal features and major tectonic features from west to east across Bangladesh and the IBR. The red color indicates volcanoes. Modified from Bandyopadhyay (2019). Representation of West-East section of Figure 2.

Across the IBR, there are some formation groups that we can identify, corresponding to different depositional settings in the fluvial-deltaic system. The Surma Group from the Miocene is in the outer belt and consists of shallow marine deposits. The Topham Group from the Miocene-Pliocene has fluvial deposits from distributary channels and braided river channels. Subsequently, floodplains, meandering rivers, and alluvial deposits make up the Dupi Tila Group from Pliocene-Quaternary. The Barail Group from the Oligocene comprises a fan depositional environment. The lack of consolidation of the sediment material of GDB means it is highly susceptible to

liquefaction and strong ground motion when an earthquake occurs. The deposition rate causes the GBD to be overpressured, mainly because of the coarser grains over finer grains with low permeability (Steckler et al., 2008).

2.4 Previous geophysical studies

A study by Rahman et al. in 2015 of the shear wave velocity of geological materials at 30 m depth in Dhaka City uses different techniques like downhole seismic and multichannel analysis of surface waves, among others. They determined that the shear wave velocity varies from 127 m/s to 295 m/s (Rahman et al., 2015). Wang et al. (2019) used seismic broadband data from southeastern Bangladesh to analyze the shear wave velocity from the Myanmar region. They mention that the Bengal Basin has a depth of around 10-15 km with a low-velocity layer that decreases from west to east near 10 km depth. According to their results, the velocity in our zone of interest in eastern Bangladesh at depths of ~15 km varies from 2 – 4 km/s (Wang et al., 2019).

CHAPTER 3. DATA

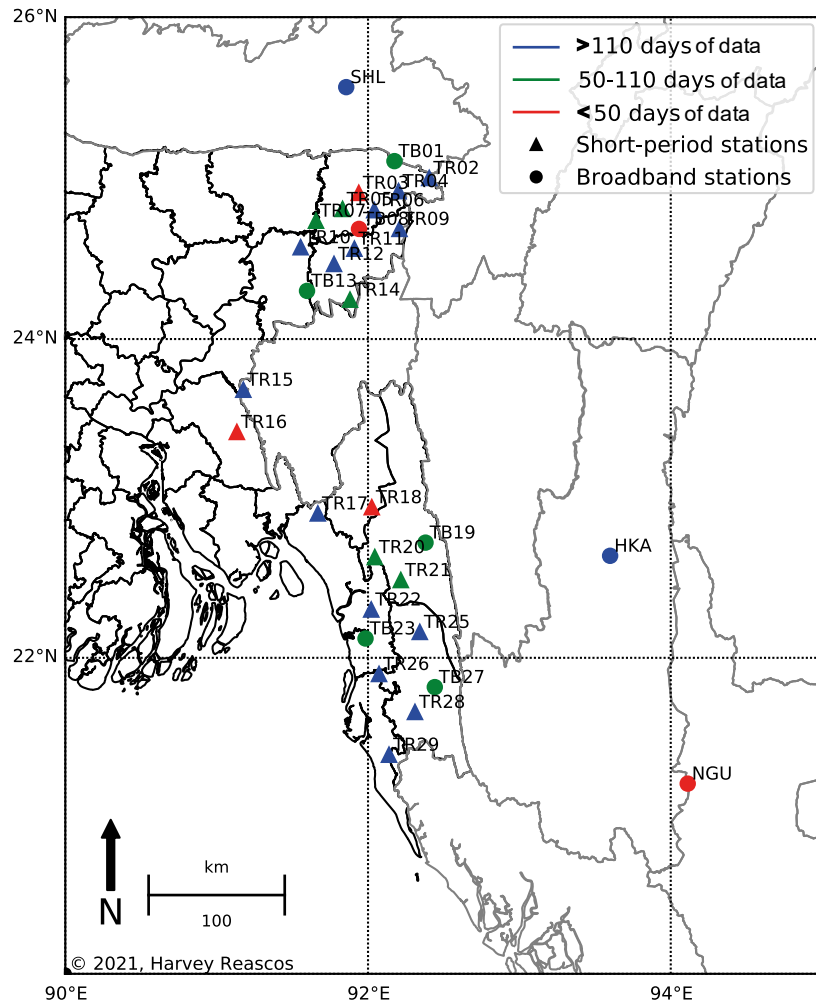


Figure 4 Seismic station locations from both broadband and short-period stations. Data available within the period January – June 2019. Sixteen stations have more than 110 days of continuous data available (blue). Ten stations have between 50 – 110 days of data (green). Five stations have less than 50 days of data (red)

We use continuous data from the seismic network "Temporary Receivers for Monitoring Bangladesh Earthquakes" (TREMBLE). The analysis's complete information comes from up to 22 short-period and six broadband seismographs deployed by the Earth Observatory of Singapore and Dhaka University from 2016 to the present in eastern Bangladesh. Additionally, we tested data from two nearby networks, IN and MM, located in northeastern India and West-Myanmar Region (Figure 4). For this study, we use six months of data that corresponds to the interval from January - June 2019 (Table 1). We collect continuous seismic data on the Z, E, and N components.

Table 1. Data for all seismic stations. Seismic network Z2 corresponds to "Temporary Receivers for Monitoring Bangladesh Earthquakes" (TREMBLE) for broadband (TB##) and short-period (TR##) stations. Additional broadband stations are from networks MM and IN. The "Start" to "End" columns represents the date range of data collected, and the number of complete days recorded is in the Days column.

| <i>Net</i> | <i>Station</i> | <i>Latitude (°)</i> | <i>Longitude (°)</i> | <i>Elev (m)</i> | <i>Start</i> | <i>End</i> | <i>Days</i> |
|------------|----------------|---------------------|----------------------|-----------------|--------------|--------------|-------------|
| Z2 | TB01 | 25.10784 | 92.17437 | 33 | Mar 01, 2019 | Apr 30, 2019 | 61 |
| Z2 | TB08 | 24.6865 | 91.94045 | 24 | Mar 28, 2019 | Apr 30, 2019 | 34 |
| Z2 | TB13 | 24.300522 | 91.59694 | 45 | Mar 01, 2019 | Apr 30, 2019 | 61 |
| Z2 | TB19 | 22.724925 | 92.379768 | 69 | Mar 01, 2019 | Apr 30, 2019 | 61 |
| Z2 | TB23 | 22.121733 | 91.983399 | 43 | Mar 01, 2019 | Apr 30, 2019 | 61 |
| Z2 | TB27 | 21.815399 | 92.441075 | 60 | Mar 01, 2019 | Apr 30, 2019 | 61 |
| Z2 | TR02 | 25.00284 | 92.40428 | 38 | Jan 17, 2019 | Jun 22, 2019 | 157 |
| Z2 | TR03 | 24.91031 | 91.93892 | 26 | Jan 16, 2019 | Jan 18, 2019 | 3 |
| Z2 | TR04 | 24.92083 | 92.20149 | 17 | Jan 17, 2019 | Jun 22, 2019 | 155 |
| Z2 | TR05 | 24.81017 | 91.83193 | 17 | Jan 16, 2019 | Jun 21, 2019 | 103 |
| Z2 | TR06 | 24.802662 | 92.04108 | 27 | Jan 16, 2019 | Jun 21, 2019 | 157 |
| Z2 | TR07 | 24.73709 | 91.65612 | 15 | Jan 15, 2019 | May 01, 2019 | 107 |
| Z2 | TR09 | 24.686125 | 92.207825 | 35 | Jan 17, 2019 | Jun 23, 2019 | 157 |
| Z2 | TR10 | 24.57194 | 91.55472 | 16 | Jan 15, 2019 | Jun 20, 2019 | 157 |
| Z2 | TR11 | 24.56283 | 91.9099 | 44 | Jan 18, 2019 | Jun 23, 2019 | 157 |
| Z2 | TR12 | 24.46795 | 91.7752 | 24 | Jan 18, 2019 | Jun 24, 2019 | 158 |
| Z2 | TR14 | 24.24517 | 91.88091 | 42 | Jan 18, 2019 | Apr 26, 2019 | 99 |
| Z2 | TR15 | 23.68256 | 91.175896 | 23 | Jan 19, 2019 | Jun 24, 2019 | 133 |
| Z2 | TR16 | 23.418579 | 91.133364 | 29 | | | 0 |
| Z2 | TR17 | 22.907652 | 91.66841 | 40 | Jan 22, 2019 | Jun 25, 2019 | 155 |
| Z2 | TR18 | 22.946944 | 92.024722 | 56 | Jan 22, 2019 | Feb 18, 2019 | 28 |
| Z2 | TR20 | 22.63361 | 92.04472 | 28 | Mar 23, 2019 | Jun 26, 2019 | 94 |
| Z2 | TR21 | 22.489148 | 92.216583 | 20 | Jan 21, 2019 | May 03, 2019 | 103 |
| Z2 | TR22 | 22.303773 | 92.021066 | 20 | Jan 24, 2019 | Jun 28, 2019 | 154 |
| Z2 | TR25 | 22.16282 | 92.341963 | 104 | Jan 23, 2019 | Jun 27, 2019 | 156 |
| Z2 | TR26 | 21.897803 | 92.072757 | 30 | Jan 24, 2019 | Jun 28, 2019 | 156 |
| Z2 | TR28 | 21.658275 | 92.31003 | 29 | Jan 23, 2019 | Jun 28, 2019 | 155 |
| Z2 | TR29 | 21.388104 | 92.138626 | 16 | Jan 23, 2019 | Jun 29, 2019 | 158 |
| MM | HKA | 22.642099 | 93.599503 | 1733 | Jan 01, 2019 | Jun 30, 2019 | 173 |

| | | | | | | | |
|-----------|-----|-----------|-----------|----|--------------|--------------|-----|
| <i>MM</i> | NGU | 21.205721 | 94.112297 | 97 | Jan 01, 2019 | Feb 24, 2019 | 18 |
| <i>IN</i> | SHL | 25.566816 | 91.855949 | 2 | Jan 01, 2019 | Jun 12, 2019 | 139 |

CHAPTER 4. METHODS

One way to get a good image of Earth's interior is by the evaluation of dispersion curves of surface waves that emerge from correlations of ambient seismic noise. The majority of energy from seismic noise is in the period range of 5 – 20 s; this allows us to obtain images that provide information on crustal and uppermost mantle structure (Cupillard et al., 2011). According to Bensen et al. (2007), there are four main steps that we have to do to measure phase velocities. (1) Prepare each station's data by accentuating the broadband ambient noise, removing the instrument response, the trend, and the mean, applying a bandpass filter, and downsampling to the desired sample rate. Then, we should use some preprocessing method to remove non-stationary signals like earthquakes or spikes that could bias the correlation. (2) Compute a cross-correlation of each time window for all station pairs, which yields in a total of $n(n-1)/2$ (n represents the number of stations). Then, stack the resulting cross-correlations together to increase the signal-to-noise ratio. For this thesis project, we decide to apply the full-stack, summing all available cross-correlations for each station pair. This process is done for both the vertical and the horizontal components after rotating into the proper radial and transverse directions for each station pair. (3) After the cross-correlation and stacking, the resulting waveform is an estimation of the Empirical Green's function (EGF), which indicates the response of the medium (Earth) to an impulse (e.g., Hutchings & Viegas, 2012). This estimate of the EGF allows us to measure the group and/or phase speeds. (4) Make an error analysis to select acceptable measurements. By applying 2D travel-time tomography, we can obtain the position-dependent phase velocity on the Earth's surface, which can then invert for shear velocity in 2D or 3D (e.g., Menke & Jin, 2015).

For this specific analysis, we will use a suite of MATLAB codes available on GitHub, called MATnoise, written by Joshua Russell and others (Russell, J., retrieved from <https://github.com/jbrussell/MATnoise>). These codes include several preprocessing options and calculate the ambient noise cross-correlation of the vertical, radial, and transverse components in the frequency domain. Considering the coherency between station pairs, one can estimate the phase velocity, then perform the inversion for 1D or 2D isotropic phase velocity maps. It has mainly been used for broadband ocean-bottom seismometer data in the past (e.g., Russell et al., 2019; Jin et al., 2015). Here, we summarize the theoretical methods used for these calculations and any changes to the short-period land-based data parameters.

4.1 Preprocessing methods

Before working with the recorded signals, we need to prepare the data. Data preparation is done using a CSH script (provided in Annex 1) and the program Seismic Analysis Code (SAC; Goldstein & Snoke, 2005). We select only records from stations with full continuous days of data. We remove the instrument response, apply a detrend function to subtract the mean of the data and a taper function to taper the ends of all traces. We apply an anti-alias zero-phase lowpass filter of 12 Hz and remove the daily oscillations using a high pass zero-phase filter of 1/60/60 Hz. After that, we downsampled our data from 100 to 20 samples per second (sps). Note that the original MAT-noise program was written for a sample rate of 1 sps; we have modified it to use data with a sample rate of 20 sps in order to make measurements at higher frequencies. We divide the data into 3-hour window segments, again detrend the data by subtracting the mean or a best-fit line from our data and apply a cosine taper to each data chunk.

Further preprocessing methods help us to remove non-stationary signals like earthquakes or spikes that could bias the correlation. We describe the four preprocessing options tested: One-bit normalization (OBN) consists of retaining just the signs (+1, -1) of each recorded sample (Cupillard et al., 2011). Time-frequency normalization (TFN) consists of filtering in narrow overlapping frequency bands within the target frequency ranges. Each narrow frequency band is treated separately and normalized to avoid strong signals at high or low frequencies. This normalization is achieved by dividing each band by its analytic time-domain envelope, producing a time series of unit amplitude. All normalized narrow frequency bands are then summed to produce the TFN (Ekström et al., 2009; Shen et al., 2012). The basic prefilter alters the seismic signals by removing the unwanted frequency signal from outside the range of our interest. For this analysis, the bandpass range is between 0.5 - 10 Hz. Additionally, we perform the calculations with no preprocessing to compare with the other methods.

The spatial correlation of the signals recorded at two stations in the frequency domain is called the cross-spectrum, and the normalized or pre-whitened cross-spectrum is called the coherency. The ambient field's coherency is proportional to the Green's function. The coherence, therefore, depends on the velocity of the ground (Yokoi & Margaryan, 2008). We calculate the coherency between each station pair for each of the preprocessing methods described above and use this value to determine the best preprocessing method for this particular data set.

4.2 Phase velocity measurements

One advantage of ambient noise correlation is that we can recover the surface waves between station pairs, and make measurements of the phase velocity at higher frequencies (>0.05 Hz) that is not possible with earthquake data (e.g., Zheng et al., 2021; Menke & Jin, 2015; Shapiro et al., 2005). The best signal to noise ratio (SNR) for ambient noise is around the frequency band of 0.1 Hz due to the microseism band's energy. The distance between the stations and the type of instrument controls the range of possible frequencies at which phase velocity measurements can be made. Time-domain methods require an interstation distance larger than three wavelengths for a given period (Menke & Jin, 2015). Frequency-domain methods are used at distances shorter than two wavelengths and with waveforms with SNR smaller than four (Shapiro et al., 2005). We, therefore, choose to use a frequency domain method following Menke & Jin (2015).

To understand the relationship between ambient noise cross-correlation and phase velocity, consider two stations, A and B, separated by a given distance. Each station will record a signal due to random noise produced in the environment. In this case, $A_p(t)$ and $B_{p'}(t)$ represent the signal received by A and B from a unique source, p. The correlation between these stations is denoted by

$$C_{AB}(t) = \sum_{p, p'} \int A_p(\tau) B_{p'}(t + \tau) d\tau \quad (1)$$

This correlation is practically (though not technically) equivalent to the Green's Function of the Earth between the two stations (e.g., Cupillard et al., 2011). Although theoretically, all seismic wave types could be retrieved this way, surface waves have the highest signal-to-noise ratio and are the most commonly studied. In this case, we will analyze the Rayleigh waves obtained from the vertical (Z) and radial (R) components.

The Bessel Function (BF) describes the cross-correlation function in the frequency domain, called the cross-spectrum, ρ . Aki (1957) used a formula to describe the vertical motion, which has a definite velocity, c , that corresponds to a given angular frequency, ω , so that the autocorrelation coefficient satisfies the following procedure:

$$\rho(\omega, r) = J_0\left(\frac{\omega_0}{c(\omega_0)} r\right) \quad (2)$$

Where J_0 is the Bessel Function, and r denotes the interstation distance. Ekström et al. (2009) used this formulation to fit the zero crossings in the observed spectrum to

the zero crossings in a BF to retrieve the phase velocity at given frequencies. Menke & Jin (2015) expanded this method to fit the BF at all frequencies. This improvement reduced the limitation of the zero-crossing process which gives poor results at low SNR. That is because noises cause bogus zeros in the observed cross-spectra, which determines the phase velocity. Menke & Jin (2015) estimate the frequency-dependent phase velocity defined by $c(\omega)$, where ω is the angular frequency recovered by the correlograms. For that, we will use the following formula for the cross-spectrum:

$$\rho(\omega, r) = AJ_0\left(\frac{\omega r}{c(\omega)}\right) \text{ with } A = 1 \quad (3)$$

They added the factor A , which is the amplitude used to model the errors and the attenuation when normalizing the cross-spectrum (in regions with strong attenuation, $A \neq 1$). The BF that best fits the observed cross-spectrum estimates the phase (Menke & Jin, 2015).

To find the phase-velocity dispersion curve, Menke & Jin (2015) first do a grid search to get an initial estimate for the starting model. We know that phase velocity typically varies smoothly with frequency, reflecting how the seismic noise waves average the Earth's structure. A phase velocity curve can thus be approximated at a few frequencies and then filled in by linear interpolation. Because of that, a grid search is successful in determining an initial model. Adjustments are then made to that starting model to find a new model that minimizes the error by least squares, a waveform fitting. Menke & Jin (2015) start building the initial model by specifying a lower and upper bound for phase velocity, c^L , and c^U , respectively. Then, the number of frequency nodes at which the phase velocity will be defined, K , and the number of phase velocity values to search for every node, L . All KL combinations are computed, and the phase velocity curve with the minimum L_2 error is selected as the starting model. After the phase velocity has been found, the amplitude A can be calculated using least squares:

$$A = \frac{[\rho^{pre}(c, A = 1)]^T \rho^{obs}}{[\rho^{pre}(c, A = 1)]^T [\rho^{obs}(c, A = 1)]} \quad (4)$$

To find the error E of all phase velocity curves, it is necessary to do four steps. (1) Interpolate it from K to N frequencies, (2) determine the BF to evaluate the predicted cross-spectrum $\rho^{pre}(c, 1)$, (3) find A using equation (4), and (4) use the equation, $e = [\rho^{obs} - \rho^{pre}(m)]$, to assess the error $E = e^T e$ (Menke & Jin, 2015). We fit the Bessel function in

the frequency range between 0.1 – 0.5 Hz.

After defining that initial model, we refine it using the least-squares method to minimize the L_2 error. We should reorder the observed cross-spectrum and unknown phase velocity as frequency series or vectors, ρ , and c , each having N values and a frequency range between ω_{min} and ω_{max} . The amplitude A and the phase velocity c join into a vector $\mathbf{m} = [c, A]$. This vector produces the typical least-squares equation $\mathbf{G}\mathbf{m} = \rho$, which is a nonlinear equation. We can linearize the equation by using the deviation from the initial model:

$$\mathbf{G}\Delta\mathbf{m} = \Delta\rho, \quad (5)$$

Where $\Delta\mathbf{m}$ is the deviation of the model from the initial model, and $\Delta\rho$ is the deviation of the observations from the initial model's predictions. \mathbf{G} contains the constraints on the model, including restrictions on the phase velocity curve's derivatives, smoothness of the phase velocity curve, and similarity to a smoothed initial model to keep values within a reasonable range. The solution is then found iteratively, and the SNR and covariance can be calculated for the final model (see Menke & Jin, 2015 for details).

4.3 Tomography

Rawlinson et al. (2010) describe seismic tomography as a method that uses information stored in seismic records to restrict 2D or 3D models of the Earth's interior. This method uses dispersive properties of the Green's Functions extracted from the ambient noise correlations (Saygin & Kennett, 2010). For this study, we apply a nonlinear 2-D tomographic inversion to get the phase velocity variations on a $0.25^\circ \times 0.25^\circ$ grid. We must also select smoothing parameters to prevent unreasonable jumps in velocity between neighboring pixels. For this, we set the isotropic second derivative equal to 100. We also apply some values for tolerance, such as the required ray density, the maximum error allowed for fitting the wavelet, the expected variance for the permitted error in the inversion, and the maximum error weight. Relative to typical broadband measurements, we have to allow higher values for the error tolerances because it is more challenging to find coherent seismic noise in the short-period seismic data. Also, we set an average velocity of 2.3 km/s on our code to calculate the wavelength for the ray tolerance and then produce the phase velocity maps.

CHAPTER 5. RESULTS

For sections 6.1 - 6.3, we use one station pair, TR02-TR05, to show all results and steps we did for short-period stations and TB01-TB08 for products we obtained with broadband stations.

5.1 Preparing data

We show examples of the raw data before and after preparing it (Figure 5 and Figure 6), as described in Section 4.1. We analyze a total of 3371 days of data.

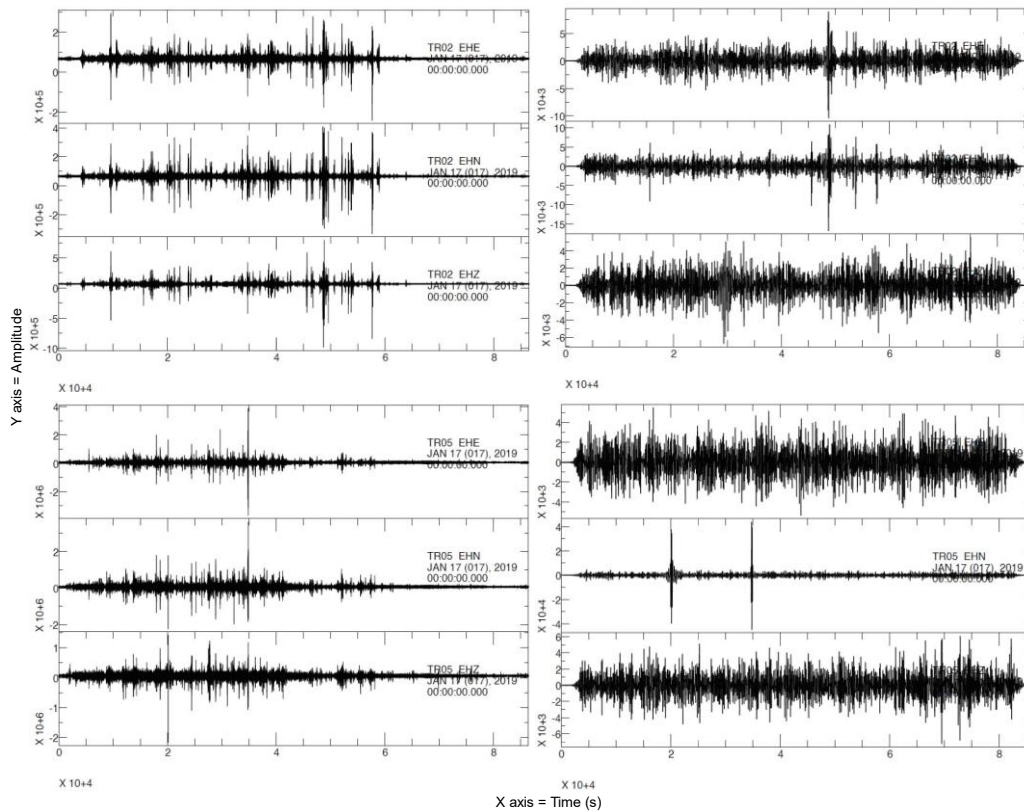


Figure 5 Continuous data for short period stations. They are TR02 (top), and TR05 (bottom), before preparing by removing the instrument response, detrending, and downsampling (left) and after preparing the data (right). Each subpanel contains three components, EHE, EHN, and EHZ, from top to bottom.

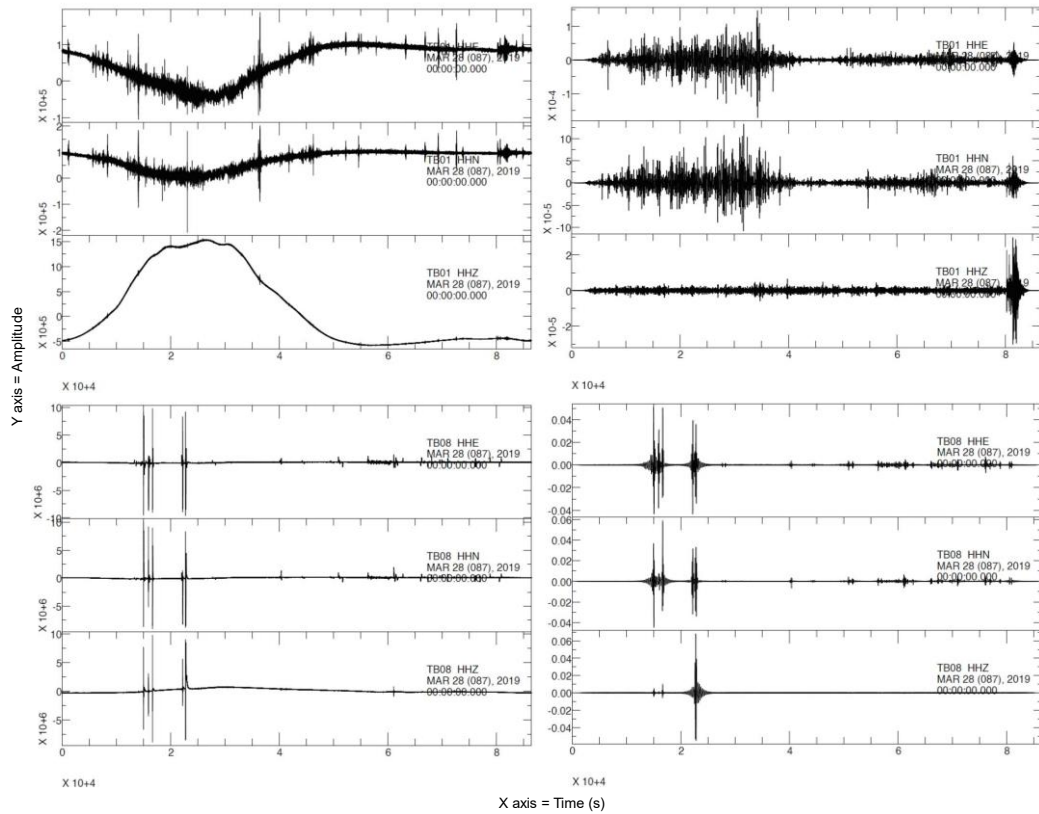


Figure 6 Continuous data for broadband stations. They are TB01 (top), and TB08 (bottom), before preparing by removing the instrument response, detrending, and downsampling (left) and after preparing the data (right). Each subpanel contains three components, EHE, EHN, and EHZ, from top to bottom.

5.2 Comparison of preprocessing methods

From the 3371 one-day files created after the preprocessing, we window the data into three-hour segments and apply the four preprocessing methods described in the methodology, section 4.1. We calculate the cross-correlation of the three-hour segments for all station pairs to get the coherency. After running all preprocessing methods, we stack all the resulting cross-correlations, reaching a total of 398 and 30 samples of coherency plots for 22 short-period stations and broadband stations, respectively (Figure 7 and Figure 8). The corresponding SNR plots are shown in Figure 9 and Figure 10.

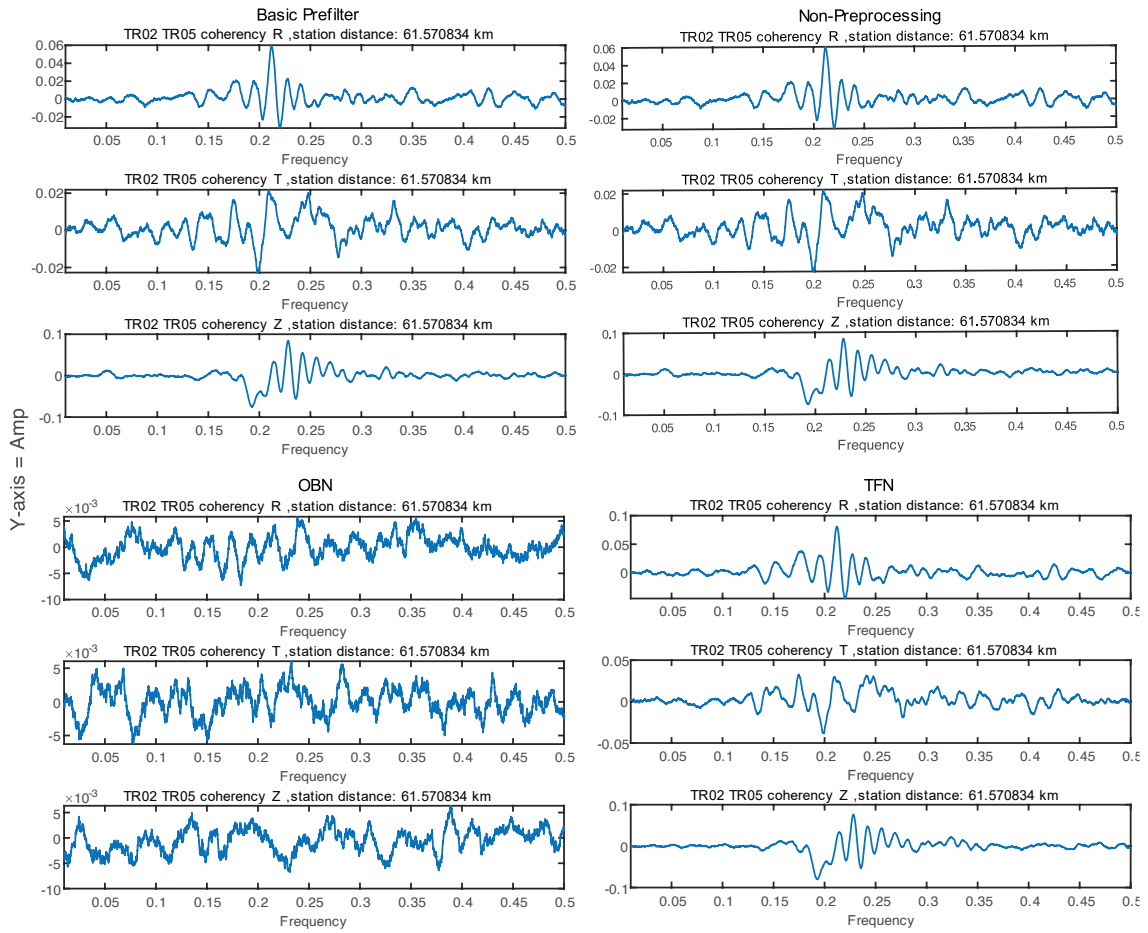


Figure 7 Coherency plots for short-period stations. It is obtained for all preprocessing methods for station pairs from short-period stations. The distance between TR02 - TR05 is about 22 km. For each graph, the coherency is shown for three components, the Radial component (R), Transverse component (T), and Vertical component (Z).

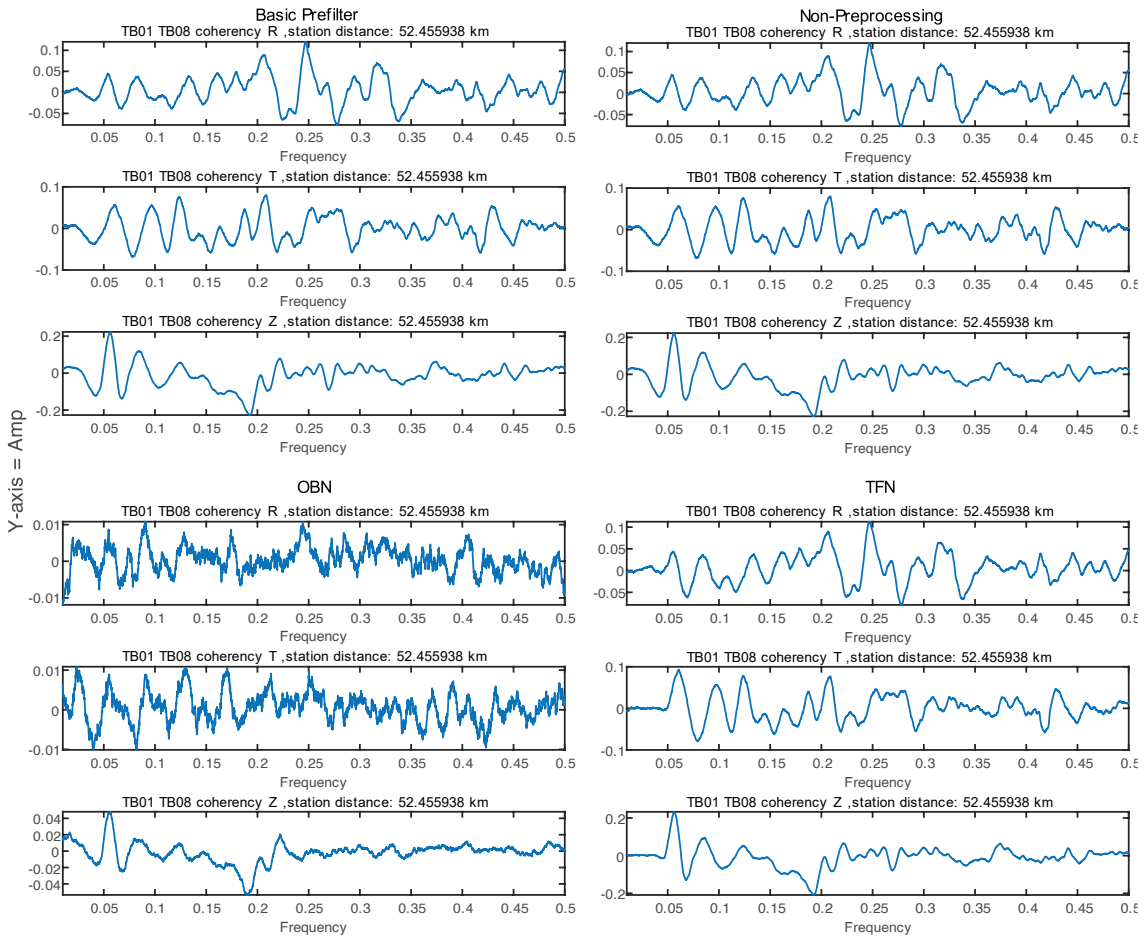


Figure 8 Coherency plots for broadband stations. It is obtained for all preprocessing methods for station pairs from broadband stations. The distance between TB01 - TB08 is about 52 km. For each graph, the coherency is shown for three components, the Radial component (R), Transverse component (T), and Vertical component (Z).

We find that the coherency plots are the worst for OBN and very similar for the other three preprocessing methods. Because TFN takes a significant amount of computational time, with little added benefit, particularly for the Z component, we also disregard this method. Based on slight advantages in the coherency and SNR, we select the BP method with a range of 2 – 10 s to use for the remainder of the processing. We set an SNR threshold of 2.5. The distances between the station pairs range from 10 km to 400 km.

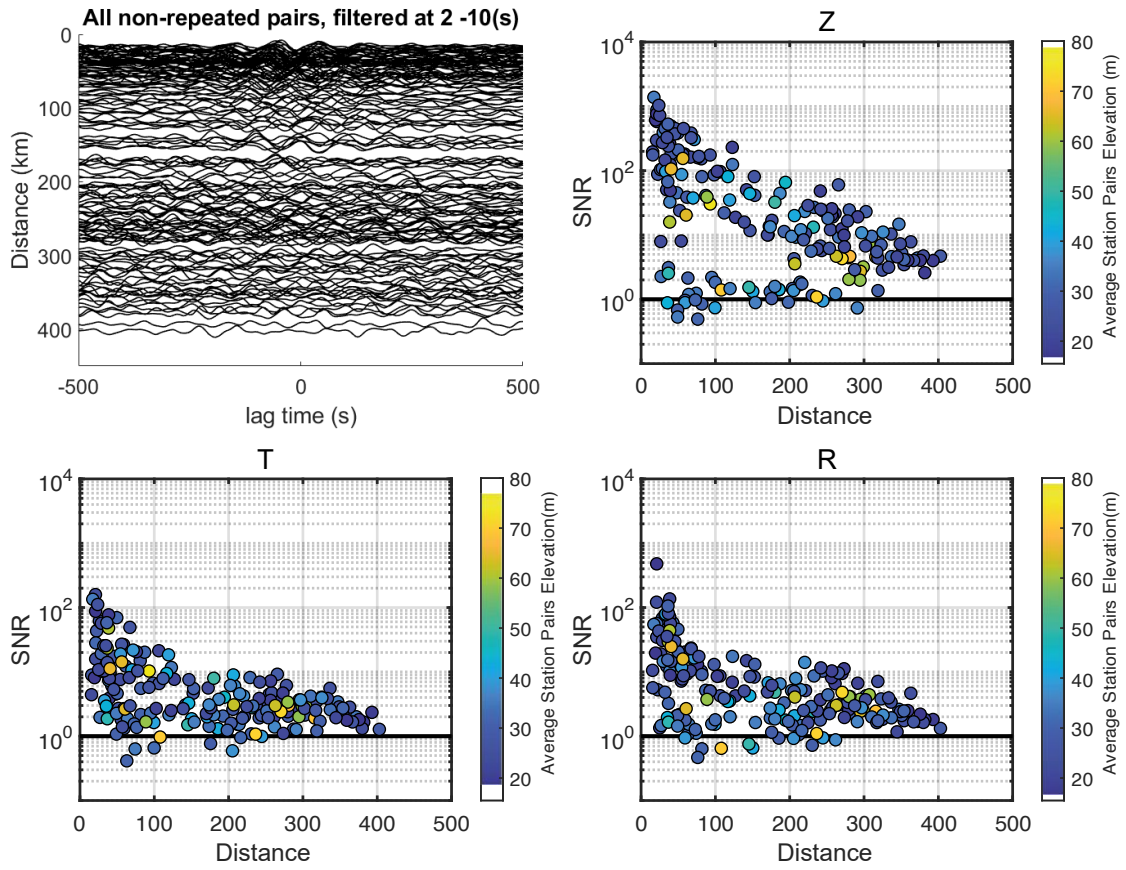


Figure 9 Cross-spectra and signal to noise ratio for short-period stations. Top left: Cross-correlations for all-non repeated pairs for short-period stations filtered at 2 – 10 s in the vertical component represented in a graph of distance (km) vs. time (s). Remaining panels: SNR vs. interstation distance for three components: Z, R, and T. We identify that the Z component has a better SNR vs. distance relationship than R and T.

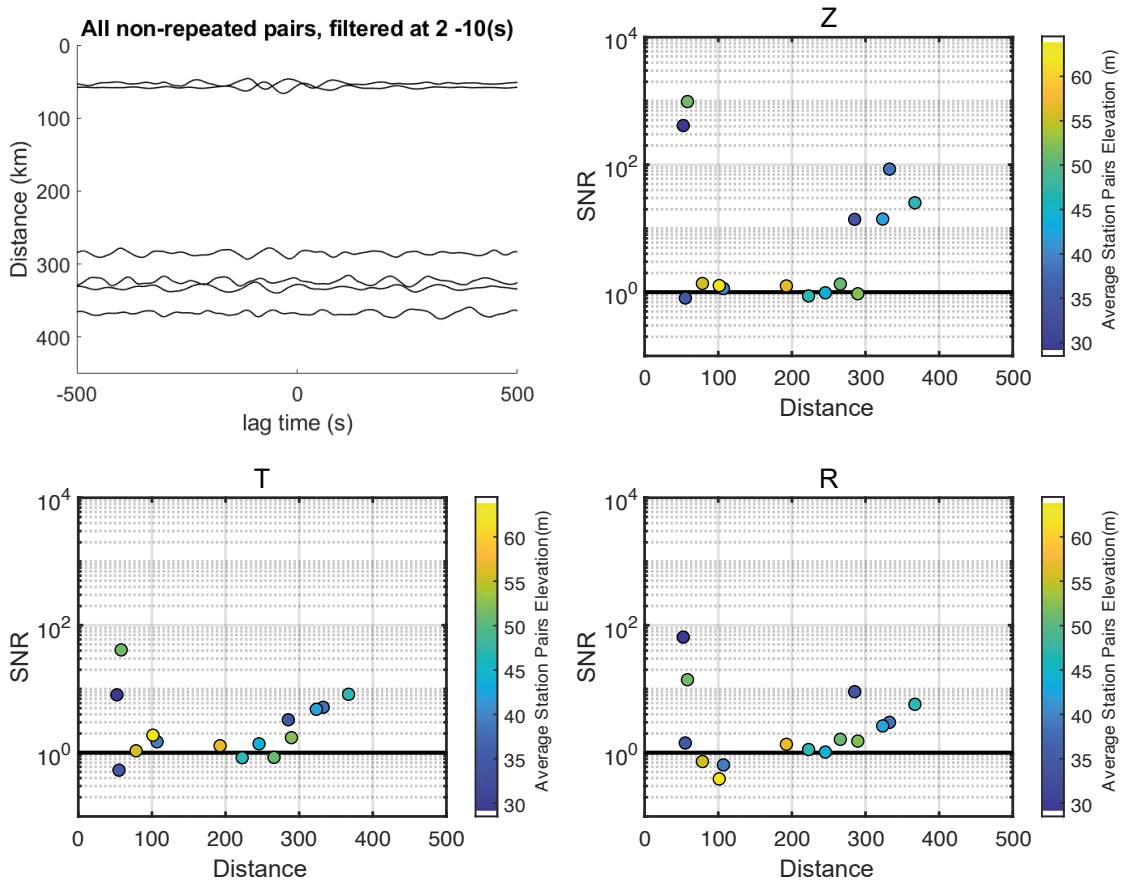


Figure 10 Cross-spectra and signal to noise ratio for broadband stations. Top left: Cross-correlations for all-non repeated pairs for broadband stations filtered at 2 – 10 s in the vertical component represented in graph of distance (km) vs. time (s). Remaining panels: SNR vs. interstation distance for three components: Z, R, and T. We identify that the Z component has a better SNR vs. distance relationship than R and T.

We make the same calculations for the broadband stations, but due to the relatively small amount of data available (two months, see Table 1), and correspondingly low SNR, we decided to work only with the short period data. Then, we generate power spectral density graphs (Figure 11) to identify the frequency content in the signal. Although the power is low throughout, the best range to estimate the phase velocities is between 2 - 10 s.

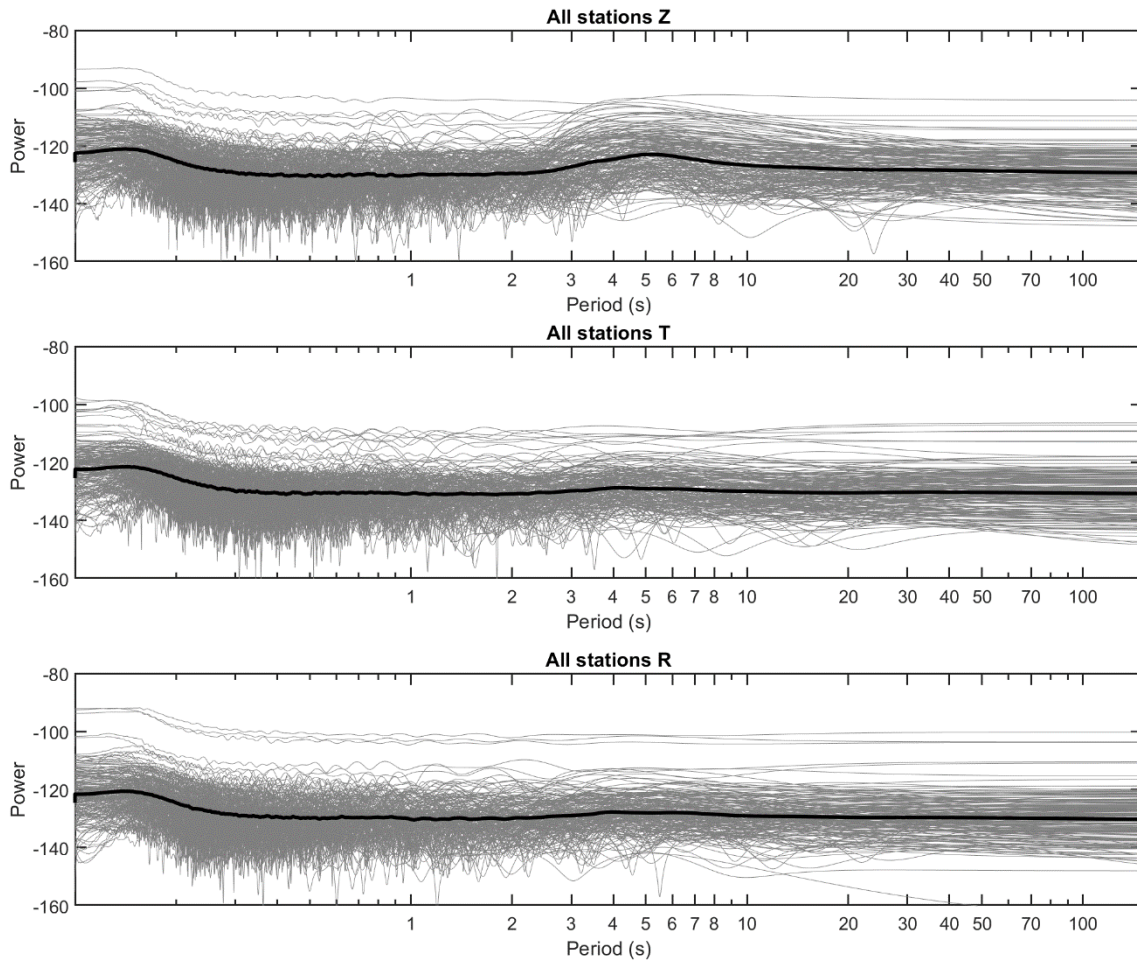


Figure 11 Power spectral density for all short period stations. It is for three components; Z, R, and T. The mean (black line) represents the average power spectrum for all cross-correlations (gray lines). On the Z component, between 2 - 10 s, there is a slight increase in power that indicates the best range of frequencies to make measurements. R and T also show a little jump between that period range, but it is minimal.

5.3 Phase velocity measurements and Bessel function

We constrain the group velocity to be between 1.4 and 4.3 km/s (Figure 12). We can observe that the Z component has a better relationship between distance vs. time because of their signal amplitudes and the symmetry in both sides of zero lag time.

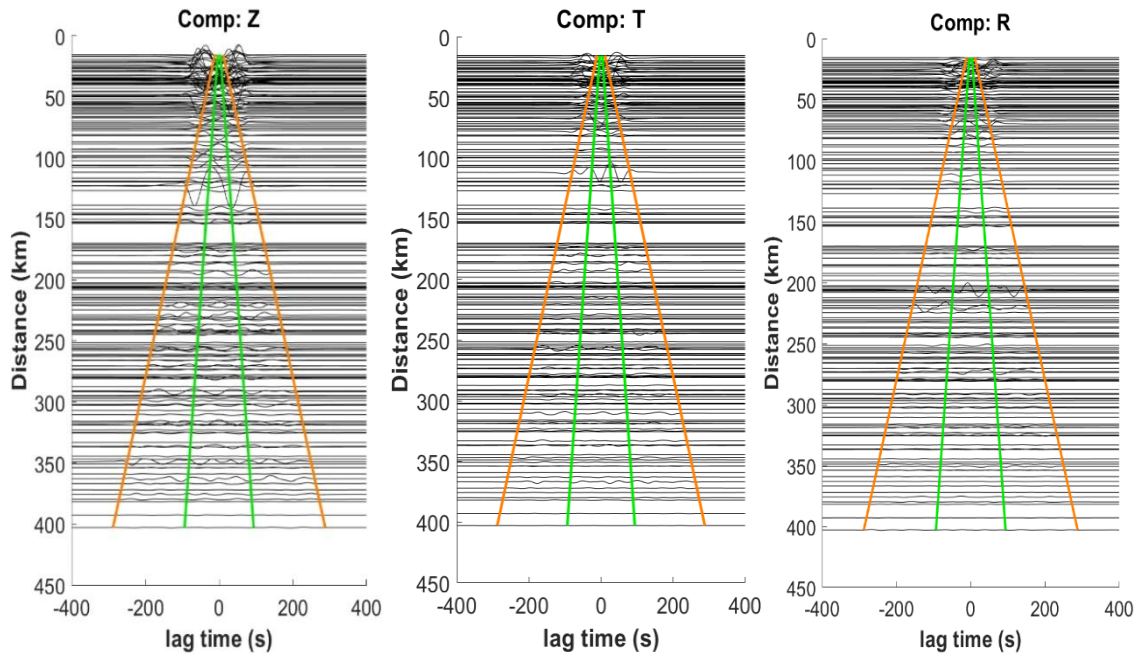


Figure 12 Group velocity window for short-period stations. It overlain on the cross-correlation functions for all station pairs, ordered by interstation distance. We can distinguish two different group velocity windows filtered at 2 – 10 s. We set the maximum group velocity (green) at ~ 4.3 km/s and the minimum group velocity (orange) at ~ 1.4 km/s.

The cross spectra evaluate where the signal is better comparing the following plots (Figure 13) in a range of 0.05 – 0.5 Hz frequency, analyzing the raw and the windowed data. The degree of bias from inhomogeneous noise sources creates the imaginary plots from the Fast Fourier Transform applied during the preprocessing methods.

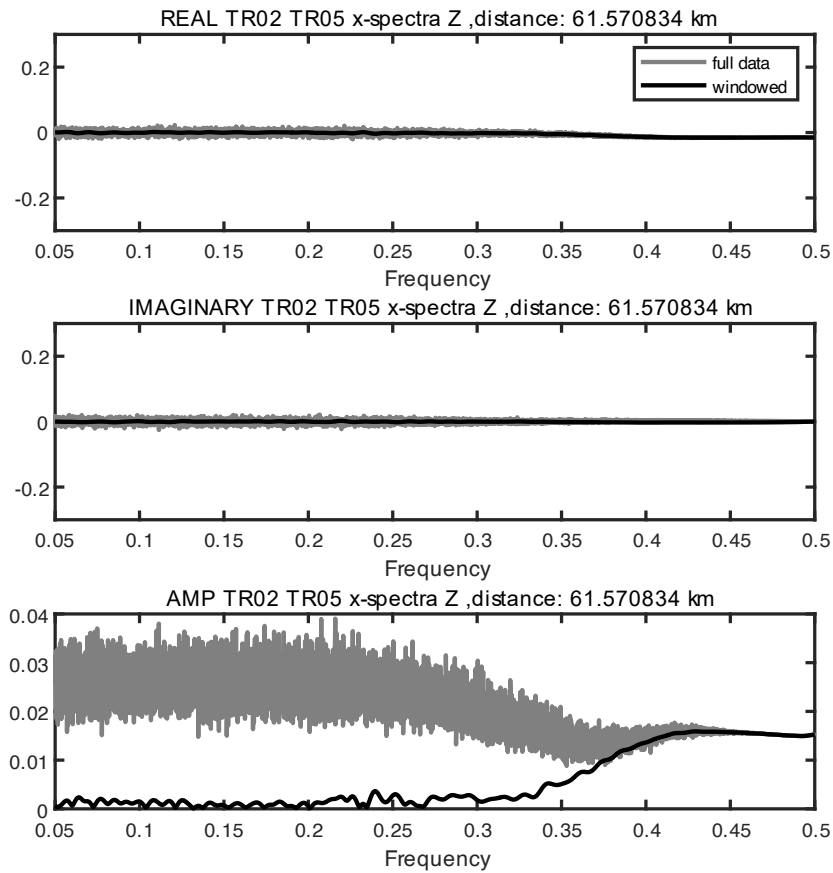


Figure 13 Real (top) and imaginary (middle) cross spectra in the vertical component. It compares the whole data (gray color) with the windowed data (black line) in a range frequency between 0,05 - 0,5 Hz. The amplitude plot shows how the noise signal is distributed: the raw data is constant near 0.03, and the window near an amplitude of zero.

Finally, we extract the phase velocity dispersion between all the station pairs to fit the normalized Bessel function at J_0 to the real cross-spectrum (Menke & Jin, 2015). To do that, we used an initial model from CRUST1.0 (Laske et al., 2013) to build the Bessel Function. We generate three different plots (Figure 14). One shows the cross-correlation between a station pair (and corresponding SNR in the title), the other is the Bessel function fit to the cross-spectrum, and the last one is the phase velocity measured for that station pair. Although the fit is poor, it is still possible to extract a phase velocity dispersion curve.

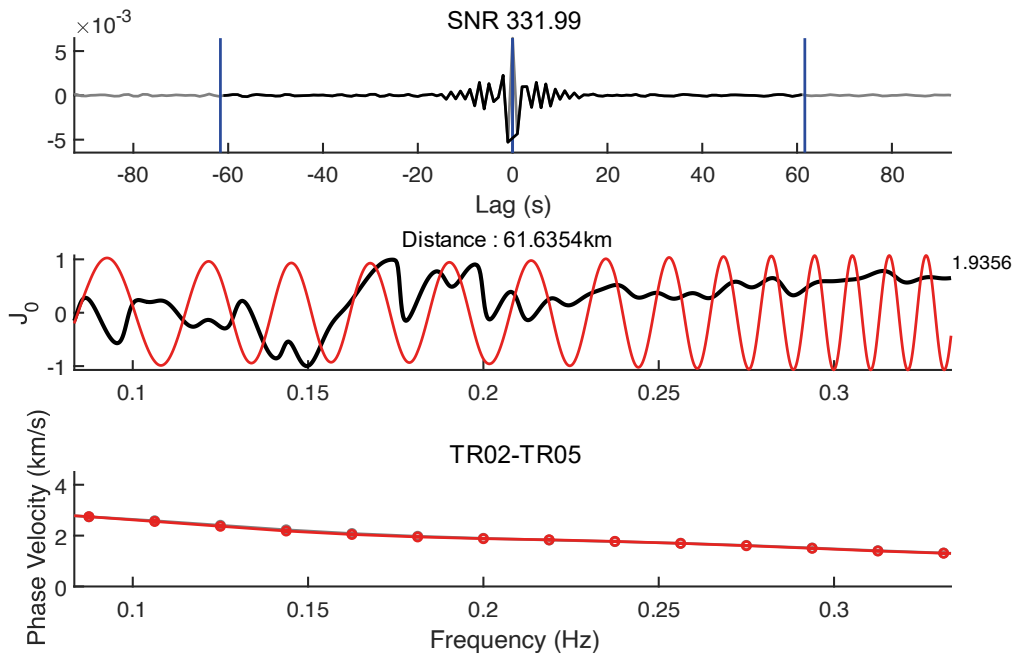


Figure 14 Cross-correlation function and corresponding SNR (top), fit of the J_0 Bessel function (red line) with the cross-spectrum (black line). The interstation distance is 61.63 km. The phase velocity measured from that station pair, TR02 - TR05, shows higher velocities at low frequencies and lower velocities at higher frequencies.

5.4 Rayleigh wave phase velocity maps

After fitting the Bessel Function, we use the phase velocity measurements to generate a ray density map (Figure 15) to know where the rays are more abundant because of the cross-correlation between them. We also calculate 2D phase velocity maps at different periods (Figure 16). We find the average isotropic phase velocity for the region (Figure 17), which closely matches the starting model.

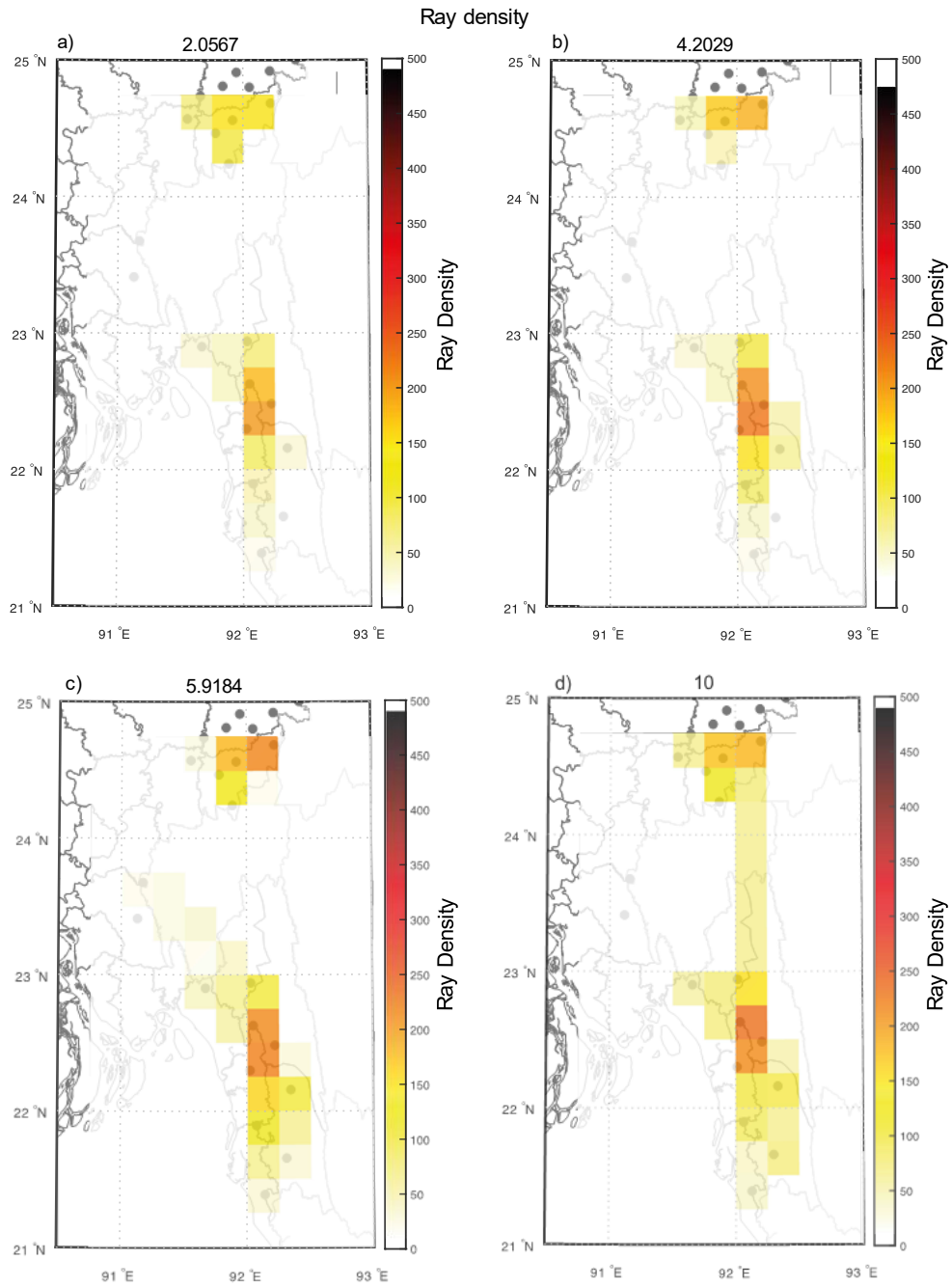


Figure 15 Ray density at different periods (approximately 2, 4, 6, and 10 s). Where there exist many crossing interstation paths, the ray density is higher (orange colors). In zones where there are fewer crossing paths, the ray density is lower.

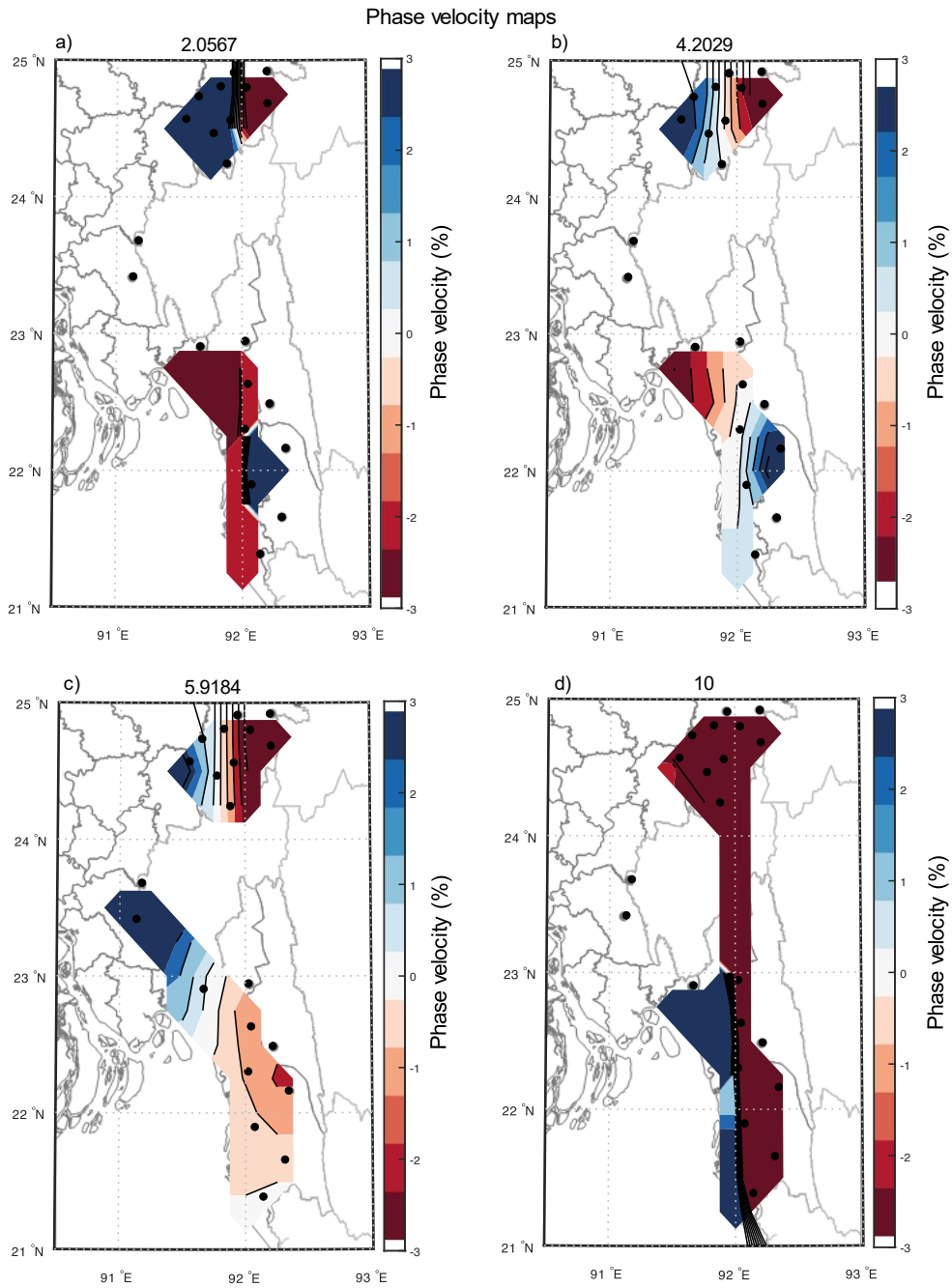


Figure 16 Phase velocity maps at different periods (approximately 2, 4, 6, and 10 s). The range for phase velocities varies from -3 to 3 % variation from the regional average (see Figure 17).

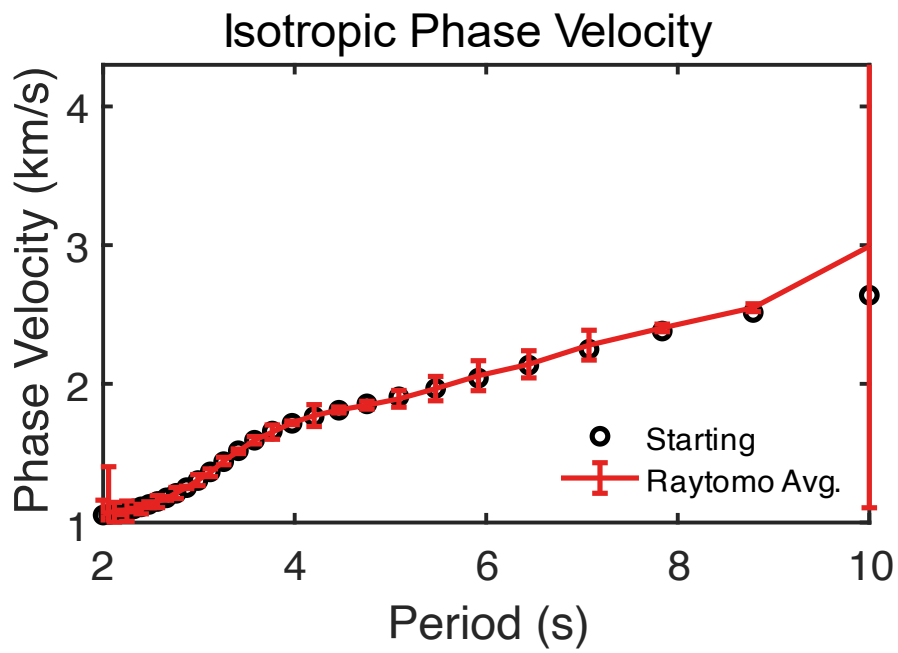


Figure 17 Average Isotropic Phase Velocity dispersion curve for all periods in a range from 2 - 10 s. The model is very similar to the initial starting model. There are slight errors near 2 s and between 5.5 – 7 s period because of the uncertainties of the phase velocity measurements.

CHAPTER 6. DISCUSSION

6.1 Quality of data

The success of using ambient noise correlations to measure phase velocities depends on noise traveling across the study area and being recorded at all stations. Both broadband and short-period seismic stations located in Bangladesh pose a particular challenge in this regard: due to the extreme thicknesses of sediments, plentiful water, and dense populations, local noise often overwhelms noise traveling across regional distances. The result of this is that the cross-correlations of signals have relatively low coherent energy to make measurements. This power represents the coherent energy at different frequencies. The average power spectral density shows shallow values at most periods, with a slight jump in the range of 2 – 10 s, where we make the phase velocity measurements. We created the cross-correlation function, and the Z component has a better notorious symmetric signal to measure the phase velocities, and it shows the expected pattern of move out; this means the lag time increases with increasing interstation distance. We also make cross-correlations for the R and T components, but it is not possible in most cases to retrieve the Green's Function to obtain the phase velocity measurements. We have had to adjust many parameters in order to make the phase velocity measurements to get some sort of fit to the Bessel Function. One crucial change was to set the grid search for an initial velocity model according to the region's expected thick and slow sedimentary layers. For this, we applied a crustal model taken from 24.5° latitude and 91.5° longitude from CRUST1.0 (Laske et al., 2013).

For the tomographic inversion, significant adjustments for tolerance were necessary, near to a value of 10000 because of the significant uncertainties associated with the phase velocity measurements. At some level, this is expected because we are using short-period stations, and these kinds of seismographs are not so efficient at analyzing the seismic noise waves. Compared to broadband stations, which are suitable for measuring ambient noise for periods >10 s, the short-period stations measure ambient noise just until 10 s (Polychronopoulou et al., 2018). Because of this, we use a frequency range for our study of [1/10 - 1/2] Hz. Additionally, Bangladesh is a difficult place to make seismic measurements on any seismometer type due to the thick sediments that trap and reverberate noise and the necessity of locating instruments in or near houses. This increases local noise at the expense of regional noise that can be cross-correlated.

6.2 Interpretation of phase velocity maps

The presence of sediments and very low elevations influence the phase velocities that we are studying in a specific period range (2 – 10 s). The existence of faults within our study zone also affects the velocities. For this thesis project, we analyze the Rayleigh waves because of their sensitivity to the near-surface. The 2-D Rayleigh wave phase-velocity maps resulting from the tomographic inversion of the phase velocities estimated from ambient noise correlation are shown in Figure 16, with the regional average shown in Figure 17. The isotropic velocity shows some errors at 2 s and between 5.5 – 7 s periods because of the uncertainties of the phase velocity measurements. There is a huge error at a 10 s period, which can be explained because of the power spectral density that from 10 s, there are not enough signals to have good phase velocity measurements.

We expect to find similar results to Crust1.0 (Laske et al., 2013), which has three sediment layers, three crustal layers, and one layer for the uppermost mantle in this location. The sedimentary layers total 8.5 km in thickness, and the crustal layers have a thickness of ~30 km. The S-wave velocities vary from 1.07 - 2.88 km/s in the sediments and 3.44 - 3.87 km/s in the crystalline crust. Making a relationship with the sensitivity plots vs. depth (Figure 18), we can correlate that the phase velocities from shorter periods correspond to a depth of approximately 2 km, and the phase velocities from higher periods correspond to a depth between 5-20 km. Because we are using a model with an 8.5 km thick sedimentary layer, we know that the Rayleigh wave phase velocity will match more of the thick sedimentary layers.

At shorter periods from the sensitivity kernel (Figure 18), it is consistent that for ~2 s and ~4 s periods, the Rayleigh wave phase velocities travel across the materials within 2 km in depth. It means that at these periods, the phase velocity of the north group stations could represent the Sylhet Basin, and the change in phase velocity from west to east could be related to the Sylhet Fault, which, according to Figure 2, is in the south part of the seismic stations of this group. Also, in this period range, the phase velocity is faster at the west than at the east because of the shallow bedrock that exist in that zone where the wave velocity exceeds ~350 m/s (Ansary & Islam, 2008). Then, the phase velocity map of the south group of stations covers a larger area, and, according to Figure 2, the faster phase velocities in the east could match with the Chin Hills and the Kaladan Fault because of the rigid material at shallow surface by the presence of anticlines along that area. These short-period results are mostly represented above the décollement (up to 3km

depth), as Betka et al. (2018) mentioned.

At longer periods, from the sensitivity kernel (Figure 18), it is for ~6 s and 10 s, the Rayleigh wave phase velocities travel across the materials between ~4 – 11 km depth and ~5 - 20 km, respectively. According to the tectonic setting, the north group stations' phase velocity could also match the same geological features as the short periods, the Sylhet Basin and the Sylhet Fault, because the average velocity is the same, faster to the west and slower to the east. From here, in a period ~6 s, we can think about the depth of sediments that fill the Sylhet Basin, which is maybe ~8 km, because at higher periods (10 s), the average phase velocity increases considerably in that zone. Furthermore, the south group stations' phase velocity covers a large area according to the ray density paths (Figure 15). So, the phase velocities in this area until ~6 s period could cover part of the Tripura fold-belt, as shown in Figure 3, which has a maximum depth of ~10 km. The same for the phase velocity at 10s shows us that the sediment layers could extend until a depth of ~20 km. Also, for both ~6 s and 10 s, the phase velocity is faster to the west, ~3%, and slower to the east, ~3%. The changes in phase velocity at longitude ~92.5°E might represent the location of the Indo-Burma subduction zone, which in Figure 1 matches it at ~93°E.

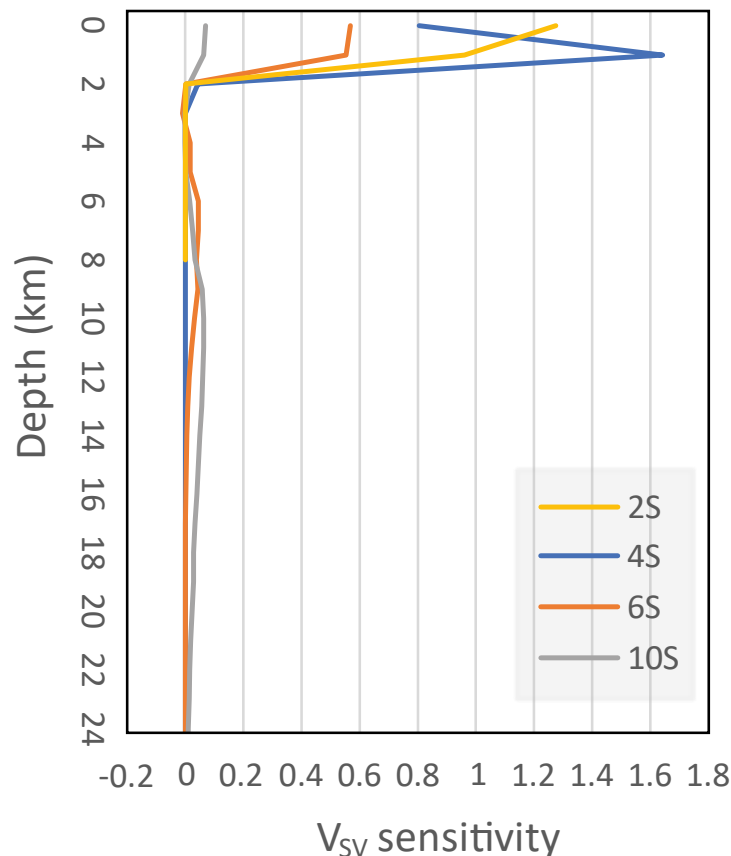


Figure 18 Sensitivity Kernels for Rayleigh waves. It is calculated for model CRUST1.0 at the location 24.5° latitude, 91.5° longitude (Laske et al., 2013; Ritzwoller, n.d.). The sensitivity of surface waves at different periods (2 s, 4 s, 6 s, and 10 s) varies in depth. It shows that the sensitivity tends to be shallower at shorter periods, covering an area of $\sim 0 - 2$ km. For longer periods, the sensitivity is deeper, covering an area between $\sim 4 - 22$ km.

After this analysis, we might infer what zones could be more susceptible to risk and hazards in case of earthquakes of high magnitude. Then, we can propose some measures to minimize the dangerous and damaging impact with some essential steps: secure the space identifying hazards, organize disaster supplies, and of course, help each other in the community.

CHAPTER 7. CONCLUSIONS

In this study, we estimate 2-D Rayleigh wave phase velocity maps. For that, we use 22 short-period stations in Eastern Bangladesh from the TREMBLE network, which we prepare by filtering, removing the instrumental response, and downsampling to 20 samples per second. After that, we test multiple preprocessing methods and select the Basic Prefilter because of the efficiency and good results in the coherency and SNR. The cross-spectra and SNR plots give us the confidence to continue working with our data because most interstation distances are above a signal-to-noise ratio of 10. In the group velocity plot, we noted that the vertical component (Z) shows us a better correlation than horizontal components (R, T), so we decide to continue working with the Z component. We select a frequency range of $[1/10 \ 1/2]$ to retrieve the Green's Function based on the power spectral density plots. This frequency range was used to fit the Bessel Function and obtain the phase velocity measurements. The resulting measurements have significant uncertainties. Because of this, we have had to set parameters with a large tolerance for errors during the 2D phase velocity map inversion, but, nevertheless, we can generate good results for tomography, and we can recognize the large-scale geological features with our phase velocity maps.

From the 2-D phase velocity maps, we note a good relationship between the phase speeds and the geological structure in eastern Bangladesh. There are significant uncertainties of the phase speed at different periods because of the lack of ray paths between station pairs. In general, at the shortest periods and shallowest depths (0 - 2 km), the estimated phase speeds are ~3% faster in the northwestern part and ~3% slower in the northeastern region. The phase velocities are 3% slower to the west and 3% faster to the east in the southern region. At 6 - 10 s period and ~5 - 20 km depth, the phase speeds are 3% faster in the west part and 3% slower in east part in both north and south region with an exception in the northern region for 10 s period which presents 3% slower phase velocity in the majority of the area. The difference in velocities depends on the different periods and geological terrain we see; for example, by the presence of bedrocks or rigid material, the waves travel faster than in softer or denser material.

Finally, it is essential to note that there are no previous studies like this in Bangladesh. This study could help better understand what tectonic setting and layers' depth we are showing in our coverage area, and with improved results, we could use it to apply some methods to reduce risk and hazards related to earthquakes, flooding, or others.

We could do it by having safety plans and raising awareness about what steps follow in case of earthquakes.

7.1 Future work

The results of this study, while an important step, have considerable uncertainties. We plan to continue improving these results. It means adding more data for short-period stations and working with the broadband stations, increasing from six months to at least one year of data and testing different stacks for the data instead of just full-stack. Then, to improve our data's quality control, we can work only with higher energy cross-correlations between station pairs, do visual quality control of the prepared data, and check individual power spectral density curves for each station pair to know if there are reasonable frequency ranges to analyze our data. Also, we will try to fit better the Bessel Function, testing different phase velocity starting models, trying other filter options, adjustments, and normalizations. These should reduce the uncertainties generated in our present studies and generate better 2-D tomography results because they will cover larger areas with ray paths.

REFERENCES

- Acharyya, S. K. (2010). Tectonic Evolution of Indo-Burma Range with Special Reference to Naga-Manipur Hills. *Memoir of the Geological Society of India*, 75, 25–43.
- Alam, E., & Dominey-Howes, D. (2014). An analysis of the AD1762 earthquake and tsunami in SE Bangladesh. *Natural Hazards*, 70(1), 903–933. <https://doi.org/10.1007/s11069-013-0841-5>
- Ansary, M. A., & Islam, M. R. (2008). Seismic Microzonation of Sylhet City. *Seismic Microzonation of Sylhet City*, 1(1), 179–195.
- Artemieva, I. M., & Meissner, R. (2012). Crustal thickness controlled by plate tectonics: A review of crust-mantle interaction processes illustrated by European examples. *Tectonophysics*, 530–531(February 2012), 18–49. <https://doi.org/10.1016/j.tecto.2011.12.037>
- Bandyopadhyay, S. (2019). Sundarban: A Review of Evolution & Geomorphology. *World Bank Group. Washington, DC*, 36.
- Bensen, G. D., Ritzwoller, M. H., Barmin, M. P., Levshin, A. L., Lin, F., Moschetti, M. P., Shapiro, N. M., & Yang, Y. (2007). Processing seismic ambient noise data to obtain reliable broadband surface wave dispersion measurements. *Geophysical Journal International*, 169(3), 1239–1260. <https://doi.org/10.1111/j.1365-246X.2007.03374.x>
- Betka, P. M., Seeber, L., Thomson, S. N., Steckler, M. S., Sincavage, R., & Zoramthara, C. (2018). Slip-partitioning above a shallow, weak décollement beneath the Indo-Burman accretionary prism. *Earth and Planetary Science Letters*, 503, 17–28. <https://doi.org/10.1016/j.epsl.2018.09.003>
- Condie, K. C. (2016). The Crust. In *Earth as an Evolving Planetary System*. <https://doi.org/10.1016/b978-0-12-803689-1.00002-x>
- Cupillard, P., Stehly, L., & Romanowicz, B. (2011). The one-bit noise correlation: A theory based on the concepts of coherent and incoherent noise. *Geophysical Journal International*, 184(3), 1397–1414. <https://doi.org/10.1111/j.1365-246X.2010.04923.x>
- Hutchings, L., & Viegas, G. (2012). Application of Empirical Green's Functions in Earthquake Source, Wave Propagation and Strong Ground Motion Studies. In G. V. E.-S. D'Amico (Ed.), *Earthquake Research and Analysis - New Frontiers in Seismology* (pp. 87–140). InTech. <https://doi.org/10.5772/28189>

- Islam, M. S., & Alam, M. J. (2009). Geological Aspects of Soil Formation of Bangladesh. *Proceedings of Bangladesh Geotechnical Conference (BGC-2009), Dhaka, Bangladesh, December 2009*, 174–183.
- Jin, G., Gaherty, J. B., Abers, G. A., Kim, Y., Eilon, Z., & Buck, W. R. (2015). Crust and upper mantle structure associated with extension in the Woodlark Rift, Papua New Guinea from Rayleigh-wave tomography. *Geochemistry, Geophysics, Geosystems*, 16(11), 3808–3824. <https://doi.org/10.1002/2015GC005840>
- Johnson, S. Y., & Nur Alam, A. M. (1991). Sedimentation and tectonics of the Sylhet trough, Bangladesh. *Geological Society of America Bulletin*, 103(11), 1513–1527. [https://doi.org/10.1130/0016-7606\(1991\)103<1513:SATOTS>2.3.CO;2](https://doi.org/10.1130/0016-7606(1991)103<1513:SATOTS>2.3.CO;2)
- Laske, G., Masters, G., Ma, Z., Pasyanos, M. E., & Livermore, L. (2013). *EGU2013-2658 Update on CRUST1.0: A 1-degree Global Model of Earth's Crust*. 2658. <https://igppweb.ucsd.edu/~gabi/crust1/laske-egu13-crust1.pdf>
- Maurin, T., & Rangin, C. (2009). Structure and kinematics of the Indo-Burmese Wedge: Recent and fast growth of the outer wedge. *Tectonics*, 28(2), 1–21. <https://doi.org/10.1029/2008TC002276>
- Menke, W., & Jin, G. (2015). Waveform fitting of cross spectra to determine phase velocity using aki's formula. *Bulletin of the Seismological Society of America*, 105(3), 1619–1627. <https://doi.org/10.1785/0120140245>
- MoDMER. (2015). Seismic Risk Assessment in Bangladesh for Bogra, Dinajpur, Mymensingh, Rajshahi, Rangpur and Tangail City Corporation / Paurashava Areas, Bangladesh. In *ATLAS, Ministry of Disaster Management and Relief* (pp. 1–229). <http://www.bd.undp.org/content/dam/bangladesh/docs/Publications/Pub2016/Seismic Risk Assessment in Bangladesh.pdf>
- Mooney, W. D. (2015). Crust and Lithospheric Structure - Global Crustal Structure. In *Treatise on Geophysics: Second Edition* (Vol. 1). Published by Elsevier Inc. <https://doi.org/10.1016/B978-0-444-53802-4.00010-5>
- Nakata, N., Gualtieri, L., & Fichtner, A. (2019). Seismic Ambient Noise. In N. Nakata, L. Gualtieri, & A. Fichtner (Eds.), *Cambridge University Press* (Vol. 58, Issue 12). Cambridge University Press. <https://doi.org/10.1017/9781108264808>
- Physics, W. (2019). Seismic Ambient Noise. In N. Nakata, L. Gualtieri, & A. Fichtner

(Eds.), *Seismic Ambient Noise*. Cambridge University Press.
<https://doi.org/10.1017/9781108264808>

Polychronopoulou, K., Lois, A., Martakis, N., Chevrot, S., Sylvander, M., Diaz, J., Villaseñor, A., Calassou, S., Collin, M., Masini, E., Bitri, A., & Stehly, L. (2018). Broadband, short-period or geophone nodes? Quality assessment of Passive Seismic signals acquired during the Maupasacq experiment. *First Break*, 36(4), 71–76.
<https://doi.org/10.3997/1365-2397.N0085>

Rabbel, W. (2006). Seismic methods. In *Groundwater Geophysics* (pp. 23–83). Springer-Verlag. https://doi.org/10.1007/3-540-29387-6_2

Rahman, M. Z., Kamal, A. S. M. M., & Sumi, S. (2015). Mapping of near surface shear wave velocity for seismic microzonation of Dhaka City, Bangladesh. *Geotechnical and Geological Engineering*, July.

Rakshit, R., Bezbaruah, D., & Bharali, B. (2018). Oblique slip faulting associated with evolving central Indo-Burmese region from Early Pleistocene deformational sequences. *Solid Earth Sciences*, 3(3), 67–80. <https://doi.org/10.1016/j.sesci.2018.04.002>

Rangin, C., Maurin, T., & Masson, F. (2013). Combined effects of Eurasia/Sunda oblique convergence and East-Tibetan crustal flow on the active tectonics of Burma. *Journal of Asian Earth Sciences*, 76, 185–194. <https://doi.org/10.1016/j.jseaes.2013.05.018>

Rashid, T. (2014). *SPRINGER BRIEFS IN OCEANOGRAPHY Holocene Sea-level Scenarios in Bangladesh*. <http://www.springer.com/series/11754>

Rawlinson, N., Pozgay, S., & Fishwick, S. (2010). Seismic tomography: A window into deep Earth. *Physics of the Earth and Planetary Interiors*, 178(3–4), 101–135.
<https://doi.org/10.1016/j.pepi.2009.10.002>

Region, A. (1984). *Northeast India, Myanmar, Bangladesh and Andaman-Sumatra Region 6.1*.

Ritzwoller, M. H., Lin, F. C., & Shen, W. (2011). Ambient noise tomography with a large seismic array. *Comptes Rendus - Geoscience*, 343(8–9), 558–570.
<https://doi.org/10.1016/j.crte.2011.03.007>

Rivet, D., Campillo, M., Sanchez-Sesma, F., Shapiro, N. M., & Singh, S. K. (2015). Identification of surface wave higher modes using a methodology based on seismic noise and coda waves. *Geophysical Journal International*, 203(2), 856–868.

<https://doi.org/10.1093/gji/ggv339>

Russell, J. B., Gaherty, J. B., Lin, P. Y. P., Lizarralde, D., Collins, J. A., Hirth, G., & Evans, R. L. (2019). High-Resolution Constraints on Pacific Upper Mantle Petrofabric Inferred From Surface-Wave Anisotropy. *Journal of Geophysical Research: Solid Earth*, *124*(1), 631–657. <https://doi.org/10.1029/2018JB016598>

Sadeghisorkhani, H. (2017). *Analyses and Application of Ambient Seismic Noise in Sweden* (Issue July).

Sarraz, A. (2015). Seismic Vulnerability Assessment of Existing Building Stocks at Chandgaon in Chittagong City, Bangladesh. *American Journal of Civil Engineering*, *3*(1), 1. <https://doi.org/10.11648/j.ajce.20150301.11>

Saygin, E., & Kennett, B. L. N. (2010). Ambient seismic noise tomography of Australian continent. *Tectonophysics*, *481*(1–4), 116–125. <https://doi.org/10.1016/j.tecto.2008.11.013>

Schimmel, M., Stutzmann, E., Arduin, F., & Gallart, J. (2011). Polarized Earth's ambient microseismic noise. *Geochemistry, Geophysics, Geosystems*, *12*(7), 1–14. <https://doi.org/10.1029/2011GC003661>

Shapiro, N., Campillo, M., Stehly, L., & Ritzwoller, M. (2005). High-resolution surface-wave tomography from ambient seismic noise. *Science*, *307*(5715), 1615–1618. <https://doi.org/10.1126/science.1108339>

Singh, A., Bhushan, K., Singh, C., Steckler, M. S., Akhter, S. H., Seeber, L., Kim, W. Y., Tiwari, A. K., & Biswas, R. (2016). Crustal structure and tectonics of Bangladesh: New constraints from inversion of receiver functions. *Tectonophysics*, *680*(May), 99–112. <https://doi.org/10.1016/j.tecto.2016.04.046>

Steckler, M. S., Akhter, S. H., & Seeber, L. (2008). Collision of the Ganges-Brahmaputra Delta with the Burma Arc: Implications for earthquake hazard. *Earth and Planetary Science Letters*, *273*(3–4), 367–378. <https://doi.org/10.1016/j.epsl.2008.07.009>

Stoker, M. S., Pheasant, J. B., & Josenhans, H. (1997). Seismic Methods and Interpretation. *Glaciated Continental Margins*, 9–26. https://doi.org/10.1007/978-94-011-5820-6_2

Toda, S., Kaneda, H., Okada, S., Ishimura, D., & Mildon, Z. K. (2016). Slip-partitioned surface ruptures for the Mw 7.0 16 April 2016 Kumamoto, Japan, earthquake 2016

Kumamoto earthquake sequence and its impact on earthquake science and hazard assessment 4. *Seismology. Earth, Planets and Space*, 68(1). <https://doi.org/10.1186/s40623-016-0560-8>

UNESCAP. (2015). *Disaster Without Borders, Regional Resilience for Sustainable Development, Asia-Pacific Disaster Report 2015*. Available at: <http://www.unescap.org/resources/asia-pacific-disaster-report-2015> (Accessed 20 December 2015).

Wang, X., Wei, S., Wang, Y., Maung Maung, P., Hubbard, J., Banerjee, P., Huang, B. S., Moe Oo, K., Bodin, T., Foster, A., & Almeida, R. (2019). A 3-D Shear Wave Velocity Model for Myanmar Region. *Journal of Geophysical Research: Solid Earth*, 124(1), 504–526. <https://doi.org/10.1029/2018JB016622>

Yang, Y., & Ritzwoller, M. H. (2008). Characteristics of ambient seismic noise as a source for surface wave tomography. *Geochemistry, Geophysics, Geosystems*, 9(2). <https://doi.org/10.1029/2007GC001814>

Yokoi, T., & Margaryan, S. (2008). Consistency of the spatial autocorrelation method with seismic interferometry and its consequence. *Geophysical Prospecting*, 56(3), 435–451. <https://doi.org/10.1111/j.1365-2478.2008.00709.x>

Zaman, A., S, S., NJ, R., A, M. A., R, A., M, K., Tanvir MH, M., Hasan K, M., & S, B. (2018). Earthquake Risks in Bangladesh and Evaluation of Awareness among the University Students. *Journal of Earth Science & Climatic Change*, 09(07), 0–6. <https://doi.org/10.4172/2157-7617.1000482>

Zheng, L., Fan, X., Zhang, P., Hao, J., Qian, H., & Zheng, T. (2021). Detection of urban hidden faults using group-velocity ambient noise tomography beneath Zhenjiang area, China. *Scientific Reports*, 11(1), 1–12. <https://doi.org/10.1038/s41598-020-80249-6>

ANNEX

Annex 1. Data preparation code

Csh Code to prepare data using the SAC program. This code requires continuously recorded data in SAC format and the instrument response from each station in the form of a pole-zero (PZ) file.

```
#!/bin/csh
# This script will remove the instrument response from all short-period stations using sac and
the pole-zero file.
#-----
# SET directory names and paths
set P1 = /mnt/c/Users/andre/Desktop/SAC_process_data # Main directory that contains the
next three subdirectories
set PSAC = /mnt/c/Users/andre/Desktop/Broadband
set POUT = $P1/PREPDATA2
set PPZ = $P1/PZFILES
set SACPROG = /usr/local/sac/bin
set TMPP = $P1/TMPPROC_01
set year = (2019) #set year of data you want to process (all stations)
set network = (Z2)
set stations=(TB01)
set channels = (HHN HHE HHZ)
#-----
# For each station, loop through each file and process individually
foreach station ($stations)
    echo 'Temporary processing directory is ' $TMPP
    if (! -d $TMPP ) then
        mkdir $TMPP
    endif
    echo 'Output directory is ' $POUT/$network/$station
    if (! -d $POUT/$network/$station ) then
        mkdir $POUT/$network/$station
    endif
    foreach channel ($channels)
        cd $PSAC/$station/
        ls ${network}.${station}..${channel}.D.${year}.???.?????.SAC > filelist.tmp
        foreach f2 (`cat filelist.tmp`)
```

```

echo " "
echo Working on file $f2
\rm $TMPP/*
cp $PSAC/$station/$f2 $TMPP/
cd $TMPP
set instr = $PPZ/${network}.${station}.${channel}.PZ
set jday = `echo $f2 | awk 'BEGIN { FS="." } {print $7}`
set hr = "00"
set mn = "00"
set sc = "00"
set Btime = `saclst B f $f2 | awk '{printf "%d", $2}` #print as integer only
set Etime = `saclst E f $f2 | awk '{printf "%d", $2}`
#set Boffset = `echo "0 - $Btime" | bc`
#set Endoffset = `echo "86400 - $Etime" | bc`
# For now, if the file is not the full day, skip it
if ($Btime > 0 || $Etime < 86400) then
    echo "****"
    echo Skipping file $f2 , missing data
    echo "****"
    continue
endif
#-----
# make a sac macro
set SACMAC = mac.sm
# read in the file
echo r $f2 > $SACMAC
# remove instrument response
echo rmean >> $SACMAC
echo rtr >> $SACMAC
echo taper >> $SACMAC
echo transfer from polezero subtype $instr to none freqlimits .005 .01 10 30 >>
$SACMAC
# Skipping merge step because we already have only one file
#trim and fill with zeros: ALSO SKIPPING SINCE WE ARE ONLY USING
COMPLETE DAY FILES
# echo rtr >> $SACMAC
# echo taper >> $SACMAC

```

```

# echo cuterr fillz >> $$SACMAC
# echo cutim B $Boffset E $Endoffset >> $$SACMAC
echo rmean >> $$SACMAC
echo rtr >> $$SACMAC
echo taper >> $$SACMAC
# downsample, new sample rate of 20 sps
echo lp bu c 12 n 2 p 2 >> $$SACMAC # anti-alias zero phase lowpass filter,
# corner frequency is originally 0.4*sr_new
# but changed to 12 hz
echo rmean >> $$SACMAC
echo rtr >> $$SACMAC
echo taper >> $$SACMAC
echo hp bu c .00028 n 2 p 2 >> $$SACMAC # Remove daily oscillations using a
# highpass zero-phase filter with a
# corner frequency of 1/60/60
echo rmean >> $$SACMAC
echo rtr >> $$SACMAC
echo taper >> $$SACMAC
echo decimate 5 filter off >> $$SACMAC
# write out as a new sac file
echo
$POUT/$network/$station/${station}.${year}.${yday}.${hr}.${mn}.${sc}.${channel}.sac >>
write
$$SACMAC
echo " >> $$SACMAC
#-----

# run the sac macro
$$SACPROG/sac << end1
macro mac.sm
q
end1
end
end
end
#clean up, removing the temporary directory
rm -r $TMPP

```